

Unavoidable multilevel biaxial symmetry breaking in chiral hybrid liquid crystals

Jin-Sheng Wu ¹, Marina Torres Lázaro ², Souvik Ghosh ¹, Haridas Mundoor,¹
Henricus H. Wensink ² and Ivan I. Smalyukh ^{1,3,4,5,*}

¹*Department of Physics and Chemical Physics Program, University of Colorado, Boulder, Colorado 80309, USA*

²*Laboratoire de Physique des Solides–UMR 8502, Université Paris-Saclay and CNRS, 91405 Orsay, France*

³*International Institute for Sustainability with Knotted Chiral Meta Matter, Hiroshima University, Higashihiroshima, Japan*

⁴*Department of Electrical, Computer, and Energy Engineering, Materials Science and Engineering Program and Soft Materials Research Center, University of Colorado, Boulder, Colorado 80309, USA*

⁵*Renewable and Sustainable Energy Institute, National Renewable Energy Laboratory and University of Colorado, Boulder, Colorado 80309, USA*



(Received 14 April 2023; revised 17 March 2025; accepted 25 March 2025; published 10 April 2025)

Chiral nematic or cholesteric liquid crystals (LCs) are fluid mesophases with long-ranged orientational order featuring a quasilayered periodicity imparted by a helical director configuration but lacking long-range positional order. Doping molecular cholesteric LCs with strongly anisotropic uniaxial colloidal particles adds another level of complexity because of the interplay between weak surface-anchoring boundary conditions and bulk-based elastic distortions near the particle-LC interface. Using cylindrical colloidal disks and rods with different geometric shapes and surface conditions, we demonstrate that these colloidal inclusions generically exhibit biaxial orientational probability distributions which may impart anomalously strong local biaxiality onto the hybrid cholesteric LC structure. Unlike nonchiral hybrid molecular-colloidal LCs, where biaxial order emerges only at critical colloid volume fractions exceeding some uniaxial-biaxial transition value, the orientational probability of the colloidal inclusions immersed in chiral nematic hosts is unambiguously biaxial even at infinite dilution. We demonstrate that the colloids induce local biaxial perturbations within the molecular orientational order of the LC host medium which strongly enhances the weak but native biaxial order of chiral nematic LC induced by the chiral symmetry breaking of the director field. With the help of analytical modeling and computer simulations based on the Landau–de Gennes free energy of the host LC around the colloids, we rationalize the observed multilevel biaxial order and conclude that it is not only unavoidable but also strongly enhanced compared to both achiral hybrid LCs and purely molecular cholesteric LCs.

DOI: [10.1103/PhysRevE.111.045410](https://doi.org/10.1103/PhysRevE.111.045410)

I. INTRODUCTION

More than 150 years ago, the discovery of chiral nematic liquid crystals (LCs) initiated a wealth of research focused on LC mesophases characterized by chirality and long-range orientational order [1,2]. These foundational studies on the geometry and topology of chiral nematic LCs, when used as model systems, offer significant insights into physical principles relevant to more experimentally challenging fields such as particle physics and cosmology [3–12].

In contrast, biaxial nematic mesophases characterized by an orthorhombic (D_{2h}) point-group symmetry have been a major area of interest in soft-matter research since they were first theoretically put forward in 1970 [13]. However, despite the existence of soft-matter systems composed of strongly biaxial building blocks such as brick-shaped molecules, the experimental demonstration of macroscopic biaxial order in equilibrium systems has proven to be elusive. Observations of biaxial nematic order have been reported in experiments on micellar and molecular LCs created from amphiphilic and bent-core molecules, respectively

[14,15]. Recently, orthorhombic LCs with long-range biaxial order have also been identified in colloidal dispersions of highly anisotropic particles embedded in molecular host nematic LCs, known as hybrid molecular-colloidal LCs [16–18].

The relationship between chirality and biaxiality has been the subject of extensive study in LC systems [19–28]. For cholesteric LCs it has been found that a helical twist of the director field reinforces local biaxial nematic order. This means that a chiral director twist must be accompanied by the molecular building blocks exhibiting some level of biaxial order in their orientation distribution. However, in purely molecular systems, the degree of chirality-enhanced biaxiality has been predicted and experimentally observed to be relatively weak [19–26]. According to the prediction by Priest and Lubensky for single-component molecular LCs [19], the extent of biaxial order scales as $(qL_m)^2$ where $q = 2\pi/p$ with p denoting the helical pitch of the chiral nematic, and L_m the typical molecule size. Regarding hybrid molecular-colloidal LCs, no attempts have thus far been made to explore the extent of biaxial orientational symmetry breaking of anisotropic colloidal particles dispersed in a chiral molecular nematic host and the response at the level of distortions of the molecular LC near the colloid surfaces.

*Contact author: ivan.smalyukh@colorado.edu

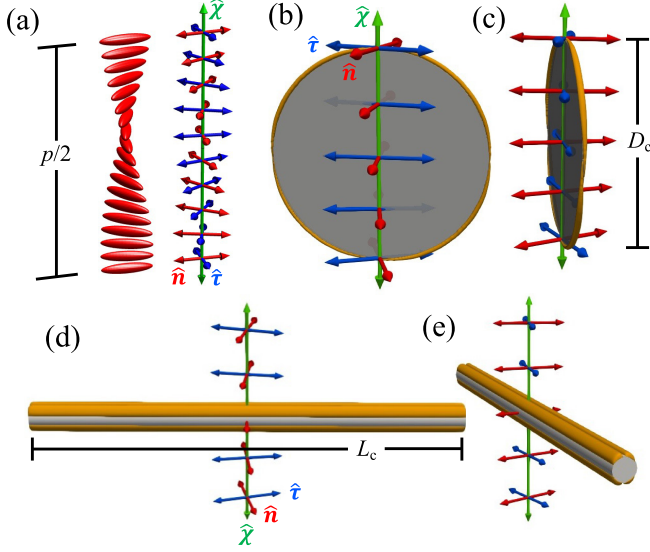


FIG. 1. (a) Chiral LC molecules (red ellipsoids) in a helical alignment spanning a half period $p/2$. The corresponding molecular frame consists of three orthogonal directors: the LC director $\hat{\mathbf{n}}$ (red), helical axis $\hat{\chi}$ (green), and a third axis $\hat{\tau}$ (blue). (b),(c) Numerical simulation of colloidal disks (gray) with perpendicular anchoring boundary conditions immersed in a chiral LC at their equilibrium orientation along $\hat{\mathbf{n}}$. The contours (orange) indicate a molecular director $\hat{\mathbf{n}}$ deviation of 0.7° away from the unperturbed helical structure. (d),(e) Simulated rods with equilibrium orientation along $\hat{\tau}$. For all simulations the anchoring at the colloidal surface is perpendicular (homeotropic) with strength $W_0 = 10^{-4} \text{ J m}^{-2}$. Cholesteric pitch $p = 10 \text{ }\mu\text{m}$, disk diameter $D_c = 1 \text{ }\mu\text{m}$, and rod length $L_c = 3 \text{ }\mu\text{m}$.

In this work, we report enhanced biaxial order for uniaxial colloidal particles dispersed in a weakly chiral molecular host [29]. The biaxial symmetry breaking is not only manifested in the orientational probability of the cylindrical colloidal particles under various boundary-anchoring conditions, it is also found to happen in the chiral molecular LC host that surrounds the colloidal particle. The ground-state symmetry of the cholesteric LC is described by three mutually perpendicular director fields (Fig. 1): the molecular director field $\hat{\mathbf{n}} = -\hat{\mathbf{n}}$ representing the local average molecular alignment, the helical axis field $\hat{\chi} = -\hat{\chi}$ along which $\hat{\mathbf{n}}$ rotates, and a third orthogonal field $\hat{\tau} = \pm\hat{\mathbf{n}} \times \hat{\chi}$, all nonpolar [30,31]. The helicoidal director configuration described by an orthogonal molecular frame ($\hat{\mathbf{n}}, \hat{\chi}, \hat{\tau}$) and helical pitch p is hardly perturbed by the introduction of thin colloidal disks or rods in view of their low concentration and weak surface-anchoring boundary conditions. The colloidal particles are shaped as uniaxial cylinders with high aspect ratios, and their preferential alignment within the molecular LC is controlled by predesigned boundary conditions at the colloid surface. We find that the colloidal orientational distribution is distinctly biaxial for both thin colloidal rods as well as for thin disks under a variety of surface-anchoring conditions. In contrast to the orientational distribution of colloidal inclusions in nematic hybrid molecular-colloidal LCs, in which biaxial order emerges only at modest to high volume fractions of anisotropic colloidal particles [17], the orientational

probability of the colloidal inclusions in chiral nematic hosts is unavoidably biaxial even at very low colloidal volume fractions. In cases where the colloids align along the $\hat{\tau}$ axis, biaxial order is found to be anomalously large, an effect that is attributed to the subtle role of weak elastic distortions of the molecular LC near the colloidal surface. We further identify that all studied cases of hybrid LC exhibit a leading-order quadratic dependency of colloidal biaxial order with molecular chirality $\Delta_{cc} \propto (qa)^2$ in line with Ref. [19] but each with different, nontrivial prefactors. At the molecular level, biaxial symmetry breaking of the LC host medium is reinforced through surface-anchoring-induced distortions emerging at the edges of the colloidal particles which enhances the weakly biaxial order that is native to any chiral LCs due to the symmetry breaking caused by the presence of the helical axis. Combining findings from experiment, computer simulation, and analytical theory we conclude that the biaxial order of chiral molecular-colloidal LCs is strongly enhanced compared to that of (achiral) nematic molecular-colloidal systems as well as compared to cholesteric molecular systems. Amplified, multiscale biaxial order is therefore a universal feature of chiral hybrid LCs. Finally, we discuss how chiral molecular-colloidal LCs may be used as powerful model systems to enable future studies of biaxial and non-abelian topological defects and solitons embedded in more complex order parameter spaces which are at present very challenging to realize.

II. METHODS AND TECHNIQUES

A. Synthesis of colloidal disks and rods

Silica microrods synthesized following an emulsion-templated wet-chemical approach [32] are adopted. To synthesize them, 1 gm of polyvinylpyrrolidone (molecular weight 40000) is dissolved in 10 ml of 1-pentanol, followed by the addition of 950 μl of absolute ethanol (Decon labs), 280 μl of deionized water, 100 μl of sodium citrate solution (0.18 M), and 130 μl of ammonia solution (28%). The bottle is shaken vigorously using a vortex mixer after each addition. Then, 100 μl of tetraethyl orthosilicate (98%) is added under agitation. The bottle is incubated at 25°C for the next 8 h. The solution becomes milky white after the reaction, and it is centrifuged at 6000 revolutions per minute (rpm) for 10 min to separate the as-synthesized rods. The precipitated rods are then washed two times with water followed by another two rounds of washing with ethanol at 3000 rpm for 5 min. Finally, to improve the monodispersity and to remove other lightweight impurities, the rods are centrifuged at 500 rpm for 30 min and dispersed in ethanol, with the procedure repeated twice. For the case of a thin colloidal disk, $\beta\text{-NaYF}_4\text{:Yb/Er}$ particles are synthesized following the hydrothermal synthesis methods described in detail elsewhere [17,18,29,33–35]. In short, 0.7 g of sodium hydroxide (from Alfa Aesar) is dissolved in 10 ml of deionized water and then 5 ml of oxalic acid solution (2 g, 19.2 mmol) and 5 ml of sodium fluoride solution (202 mg, 4.8 mmol) are added under stirring that lasts 15 min. Then, 1.1 ml of $\text{Y}(\text{NO}_3)_3$ (0.88 mmol), 0.35 ml of $\text{Yb}(\text{NO}_3)_3$ and 0.05 ml of $\text{Er}(\text{NO}_3)_3$ are added into the mixture while the stirring continues for another 20 min at room temperature. The solution is then transferred

to an oven (Col-Int Tech) and kept at 200 °C for 12 h. The mixture is cooled down naturally to room temperature after which the particles precipitated at the bottom are collected by centrifugation.

B. Surface functionalization of the colloids

Surface chemical treatment of the synthesized colloids not only provides the desired anchoring preference but also controls the particle aspect ratio. Specifically, the emulsion-templated rods are slowly etched in a mild basic condition [36] with 0.5 mM NaOH for 24 h, followed by drying at 80 °C for another 4 h. After this, the functionalization of the silica rods is done by adding 100 μ l of perfluorooctyltriethoxysilane (TCI America) to 0.9 mL ethanol dispersion of the silica rods. The mixture is kept at room temperature for 3 h before being washed and redispersed three times in ethanol. After vacuum drying inside a desiccator and heating at 60 °C for 1 h, the microrods are immersed in a perfluorocarbon liquid (Fluorinert FC-70, Alfa Aesar) and kept at 60 °C for 1 h before being cooled down to room temperature and redispersed into ethanol for storage. The fusion of perfluorocarbon oil onto the perfluorosilane functionalized rods results in a fully covered and stable slippery surface layer, giving desired boundary conditions. On the other hand, the homeotropic surface-anchoring boundary on the β -NaYF₄:Yb/Er disk surfaces is controlled through surface functionalization with a thin layer of silica and polyethylene glycol. Details are given in Ref. [18].

C. Colloidal particle dispersion in chiral molecular LC

A small amount of left-handed chiral dopant cholesterol pelargonate (Sigma Aldrich) is added into molecular 5CB (pentylcyanobiphenyl or 4-cyano-4'-pentylbiphenyl; Frinton Labs and Chengzhi Yonghua Display Materials Co. Ltd). To obtain the equilibrium pitch p of the molecular chiral mixture, the weight fraction of the chiral additive is roughly estimated using $c_d = \frac{1}{6.25p}$ with p the desired cholesteric pitch. The actual pitch is later measured using optical microscopy by observing the periodicity of defect lines in Gradjean-Cano wedge cells [37]. The surface-functionalized particles are then dispersed into such prepared molecular chiral LC. In a typical experiment, 20 μ l of colloidal dispersion in ethanol is mixed with 20 μ l of the molecular LC. The mixture is then heated to 75 °C and kept for 2 h to completely evaporate the organic solvent. A well-dispersed molecular-colloidal hybrid LC is usually obtained after quenching back to room temperature under mechanical agitation [38–40]. Additional centrifugation can be carried out to remove possible particle aggregates formed during the isotropic to chiral nematic phase transition of the molecular LC.

Hybrid LCs obtained from the colloidal dispersion are then infiltrated into glass cells with a gap thickness typically between $p/2$ and $10p$, which is experimentally set using Mylar films or silica spheres. To achieve unidirectional planar boundary conditions for the 5CB host molecules, cell substrates are coated with 1 wt.% aqueous polyvinyl alcohol and rubbed unidirectionally. Typically, the geometry and planar boundary conditions of the cell give a sample with its helical axis $\hat{\chi}$ perpendicular to the glass substrate and with the

helical twist of the cholesteric host LC in compliance with the designed boundary conditions at the confining glass surfaces.

D. Characterization of the colloidal orientations

A combination of microscopy-based studies, including photon-upconverting confocal microscopy, phase contrast microscopy, and polarizing optical microscopy, are performed using a multimodal three-dimensional (3D) nonlinear imaging system built around a confocal system FV300 (Olympus) and an inverted microscope (Olympus IX-81), with details provided in Refs. [39,41]. Briefly, upconversion luminescence signals are emitted by the β -NaYF₄:Yb/Er particles when excited with a laser light at 980 nm (80 MHz coherent from a Ti:Sapphire oscillator by Chameleon ultra). The signals are epi-collected by a 100 \times objective (Olympus UPlanFL, numerical aperture 1.4) with a set of Galvano mirrors used to adjust the focal position, providing a high 3D spatial resolution. The phase contrast images, on the other hand, are taken using a 60 \times objective (Olympus UPlanFL N, variable numerical aperture 0.65–1.25), mounted on another microscope system (Olympus IX-83), at various positions controlled by a motorized sample stage.

Analysis of the colloid orientations has been detailed in Ref. [29]. Briefly, the normal direction of disks or the long axis of rods are analyzed on two-dimensional (2D) slice images of a 3D sample with the error in measured colloidal angles about $\pm 1^\circ$. The micrographs perpendicular to the helical axis $\hat{\chi}$ reveal the azimuthal orientational distribution φ . Particles out of focal depth are discarded using processing software (imagej) based on color and brightness in phase contrast micrographs. Average azimuthal colloidal orientations are calculated from the data obtained in each \hat{n} - \hat{r} slice plane and plotted against the sample depth (z) position of the cross-sectional plane, revealing the helical twist of the colloidal axes. The corresponding helical pitch p of each 3D sample is calculated from the rotation rate of the colloidal axes across the sample depth ($\Delta\varphi/\Delta z = 360^\circ/p = q$). Finally, the colloidal orientation distribution is projected to and visualized in the molecular director coordinate system frame using $\delta = \varphi - qz$, representing the fluctuation of colloidal orientation around that of a perfect helix. Histograms of angular probability distribution with 5° bin width are calculated and numerical fitting based on the theoretical model Eq. (14) is performed. Data from the histograms and results from the fits are presented using dots and curves, respectively. Each distribution is scaled by its maximum population. In certain cases, the strength of orientational fluctuations of the colloidal particles out of the imaging plane are estimated using the free energy from the analytical model (see Results and Ref. [29]) due to the limit of vertical resolution in phase contrast microscopy. Subsequently, the colloidal orientational order parameters [Eqs. (22) and (23)] are computed based on the histogram data and are listed in Table I.

E. Computer simulation of perturbed order of the molecular LC host around the colloidal particle

Computer simulations are carried out to study the molecular LC order in the vicinity of the colloidal surface as well

TABLE I. Colloidal uniaxial (S_c) and biaxial (Δ_c) order parameters measured within the colloidal frame (second subscript c) or the molecular frame (second subscript m). Strongly enhanced biaxial order emerges for the case of homeotropic rods (in bold). In addition to the current experimental data shown in Figs. 3–5, results from a previous publication [29] are also included here.

Sample	S_{cc}	Δ_{cc}	S_{cm}	Δ_{cm}
Homeotropic disk	0.66	0.067	0.66	0.067
Planar rod	0.94	0.016	0.94	0.016
Homeotropic rod ($L_c = 1.7 \mu\text{m}$)	0.70	0.12	-0.28	0.79
Homeotropic rod ($L_c = 3.0 \mu\text{m}$)	0.80	0.018	-0.39	0.81

as its impact on colloidal orientation preference. The simulations are based on minimizing the mean-field Landau–de Gennes free energy for the molecular LC host [5,17,42–44]. The bulk free-energy density consists of thermotropic effects representing the isotropic-nematic transition of LCs and spatial derivatives associated with LC director elastic distortions occurring in the bulk volume of the LC

$$f_{\text{bulk}}^{\text{LC}} = \frac{A}{2} \mathbf{Q}_{ij}^{(m)} \mathbf{Q}_{ji}^{(m)} + \frac{B}{3} \mathbf{Q}_{ij}^{(m)} \mathbf{Q}_{jk}^{(m)} \mathbf{Q}_{ki}^{(m)} + \frac{C}{4} (\mathbf{Q}_{ij}^{(m)} \mathbf{Q}_{ji}^{(m)})^2 + \frac{L_1}{2} \left(\frac{\partial \mathbf{Q}_{ij}^{(m)}}{\partial x_k} \right)^2 + \frac{L_2}{2} \frac{\partial \mathbf{Q}_{ij}^{(m)}}{\partial x_j} \frac{\partial \mathbf{Q}_{ik}^{(m)}}{\partial x_k} + \frac{L_4}{2} \epsilon_{ijk} \mathbf{Q}_{il}^{(m)} \frac{\partial \mathbf{Q}_{kl}^{(m)}}{\partial x_j} + \frac{L_6}{2} \mathbf{Q}_{ij}^{(m)} \frac{\partial \mathbf{Q}_{kl}^{(m)}}{\partial x_i} \frac{\partial \mathbf{Q}_{kl}^{(m)}}{\partial x_j}, \quad (1)$$

with the molecular tensorial order parameter $\mathbf{Q}^{(m)}$ being a 3-by-3 matrix describing the local average molecular ordering, x_i ($i = 1, 2, 3$) the cartesian coordinates, and ϵ the 3D Levi-Civita tensor. Summation over indices is assumed. Among the LC material parameters in these bulk energy contributions, A , B , and C are thermotropic constants and L_i ($i = 1, 2, 4, 6$) are the elastic constants. LC chirality is determined by L_4 , which is inversely proportional to the cholesteric pitch p [43]. The energy induced by the boundary condition at the colloidal surfaces is expressed as [45]

$$f_{\text{surf}}^{\text{LC}} = W_0 (\mathbf{P}_{ik} \tilde{\mathbf{Q}}_{kl} \mathbf{P}_{lj} - \frac{3}{2} S_{\text{eq}}^{(m)} \cos^2 \theta_e \mathbf{P}_{ij})^2, \quad (2)$$

with W_0 the surface-anchoring strength, $\mathbf{P} = \hat{\mathbf{v}} \otimes \hat{\mathbf{v}}$ the surface projection tensor, $\hat{\mathbf{v}}$ the surface normal director, $\tilde{\mathbf{Q}} = \mathbf{Q}^{(m)} + \frac{1}{2} S_{\text{eq}}^{(m)} \mathbf{I}$, and θ_e the energetically preferred angle made by LC molecular director $\hat{\mathbf{n}}$ and surface normal direction. For instance, $\theta_e = 0$ corresponds to vertical or homeotropic anchoring at the molecular-colloidal boundary, and $\theta_e = \pi$ leads to planar degenerate anchoring.

The dimensions of the colloids and their surface-anchoring types are represented as boundary conditions within the simulation box. The interior of the colloids is irrelevant and excluded from the simulation. Typically, disks are represented by a diameter $D_c = 1 \mu\text{m}$ and thickness $L_c = 10 \text{ nm}$ for most cases while long rods have dimensions $D_c = 28 \text{ nm}$ and $L_c = 1.7 \mu\text{m}$. Integration of Eq. (1) over the box volume along with the anchoring contribution Eq. (2) running over the colloid-host interfaces produces the total bulk and surface energies for the host LC, respectively.

The molecular LC configuration under thermal equilibrium is established from minimization of the total free energy based on the forward Euler integration method

$$\frac{d\mathbf{Q}^{(m)}}{dt} = - \frac{dF_{\text{total}}^{\text{LC}}}{d\mathbf{Q}^{(m)}}, \quad (3)$$

with t being the scaled energy-relaxation time of the LC. To increase numerical efficiency and stability, the adaptive Runge-Kutta method (ARK23) and a Fast Inertial Relaxation Engine are adopted [46,47]. Once a steady-state or equilibrium structure is obtained, the molecular director $\hat{\mathbf{n}}$ is identified from the eigenvector corresponding to the largest eigenvalue of $\mathbf{Q}^{(m)}$ [42]. To model a 5CB molecular LC with chiral dopants and a $30 \mu\text{m}$ pitch the following parameters are used [17,43]: $A = -1.72 \times 10^5 \text{ J m}^{-3}$, $B = -2.12 \times 10^6 \text{ J m}^{-3}$, $C = 1.73 \times 10^6 \text{ J m}^{-3}$, $L_1 = 3.29 \times 10^{-12} \text{ J m}^{-1}$, $L_2 = 5.32 \times 10^{-12} \text{ J m}^{-1}$, $L_4 = 1.97 \times 10^{-6} \text{ J m}^{-2}$, and $L_6 = 3.52 \times 10^{-12} \text{ J m}^{-1}$.

III. RESULTS

A. Symmetry breaking at the single colloid level

The symmetry breaking of the nematic colloidal geometry, induced by the twisted alignment of chiral molecules, can be revealed at the single particle level by visualizing the LC distortion field around a single colloidal particle (Fig. 1). For cylinder-shaped particles dispersed in an isotropic fluid solvent, such as thin disks or slender rods in ethanol, a continuous rotational symmetry can be observed locally with the symmetry axis being the disk normal or the long axis of the rod because the other two orthogonal axes are geometrically equivalent. When the cylindrical colloids are dispersed into a chiral nematic, however, the uniaxial symmetry is broken in view of the boundary condition at the particle-molecule interfaces and also because of the far-field helical configuration of the molecular LC director. The rotational symmetry of the surface-defect-dressed cylindrical colloids becomes discrete (twofold rotation) once the colloids are immersed in a chiral LC even when the realigning effect induced by the boundary conditions at the colloidal surfaces is rather weak and the deviation angle is small (Fig. 1). Clearly, stronger surface-anchoring forces and higher levels of host chirality (shorter cholesteric pitch) lead to significantly stronger distortions of the molecular LC and enhanced emergent biaxiality as inferred from computer simulations of the local director field of the host LC. Remarkably, biaxial symmetry breaking at the single-particle level is observed even when the helical pitch p is much larger than the particle dimensions of 1–2 μm . This demonstrates that the shape biaxiality of the dressed colloidal particle, imparted by the molecular chirality of the host, unavoidably develops even at the weak levels of surface anchoring and molecular chirality prevalent in our experiments.

B. Orientational distribution of the colloidal particles

To analyze the equilibrium orientation of the cylindrical particles, we perform several sets of simulations at various colloidal orientations and resolve the corresponding free energies. A thin disk with perpendicular boundary condition

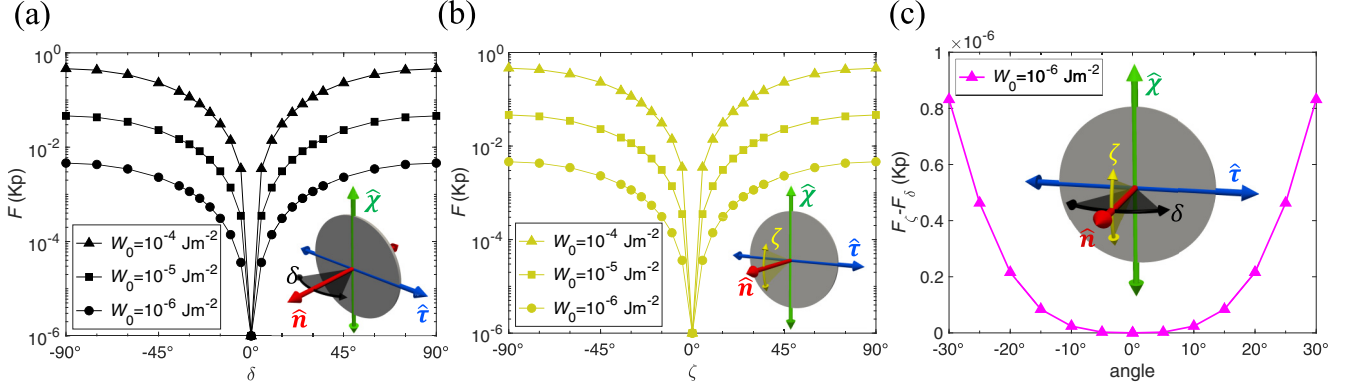


FIG. 2. (a) Free energy obtained from computer simulation of a molecular chiral LC in the presence of a homeotropic disk at different surface-anchoring strengths W_0 as a function of the azimuthal angle δ describing a rotation of the disk normal about the pitch axis $\hat{\chi}$ (green). Inset defines the molecular frame and the deviation angle δ of the disks normal away from \hat{n} towards τ . Data points for $W_0 = 10^{-4}$, 10^{-5} , and 10^{-6} J/m² are marked with triangles, squares, and circles, respectively. The energy is scaled by Kp where $K = 5.6$ pN is the average elastic constant and $p = 30$ μm the cholesteric pitch. (b) Numerical free-energy profile for a homeotropic disk rotated about $\hat{\tau}$ (blue axis). (c) The energy difference in (a) and (b) calculated for $W_0 = 10^{-6}$ J/m². The lowest energies (disk normal aligned along the red axis \hat{n} , $\delta = \zeta = 0$) for each simulation set are chosen to be $10^{-6}Kp$ instead of 0 to avoid singularities when converting to a logarithmic scale in (a) and (b). Cholesteric pitch $p = 30$ μm and disk diameter $D_c = 1$ μm for all simulations.

(Fig. 2), for example, favors alignment in which the disk normal vector orients along the molecular director \hat{n} . Deviations away from the equilibrium direction give rise to an increase in the overall free energy of the system [Eqs. (1) and (2)]. We emphasize that the free-energy profiles are distinct for the two deviation angles δ and ζ in Fig. 2 (with lower energy penalty for orientational fluctuation along δ). Though weak, the difference between the two angles and the broken uniaxial symmetry as a consequence of the chirality in the molecular LC host are unambiguous, as demonstrated empirically in Ref. [29]. Furthermore, a stronger surface-anchoring force with a higher value of W_0 leads to a more pronounced energetical nondegeneracy of the two deviation angles. Using mean-field numerical simulation of the LC host, we are able to validate the local biaxial symmetry of the orientational probability distribution of an individual colloid, arising from the inequivalence of $\hat{\chi}$ and $\hat{\tau}$ in the molecular LC host.

C. Experimental observation and analysis of the colloidal orientation

The orientational distributions obtained for thin disks dispersed in a chiral LC are shown in Fig. 3 [29]. Probed using upconversion luminescence confocal microscopy, the normal directions of the colloidal disks with homeotropic surface rotate along the sample depth [Fig. 3(a)], forming a helical alignment with a rotating rate consistent with our pre-designed cholesteric pitch $\Delta\varphi/\Delta z = 360^\circ/p$ [Fig. 3(b)]. We conclude that the low particle density ($\approx 0.026\%$ in colloidal volume fraction) guarantees a helical alignment [Fig. 1(a)] undisturbed by the introduction of the colloids. In addition, a statistical analysis of colloidal orientations in such experiments reproduces the results from the single-particle simulation demonstrated above (Fig. 2) since particle-particle interactions are insignificant. As shown in Fig. 3(c), the peak width of the δ (24.2°) orientational

distribution is larger than that in ζ (22.5°). This asymmetry in angular fluctuations suggests that homeotropically anchored disks more easily fluctuate away from \hat{n} towards $\hat{\tau}$ than towards $\hat{\chi}$, a result that is consistent with the results of the single-particle-based simulations shown in Fig. 2.

While the case of homeotropic disks has been discussed in detail in our previous work [29], here we additionally present rods with planar degenerate surface anchoring (Fig. 4), a case with a similar energy landscape in terms of particle reorientation. With the molecular director preferentially pointing parallel to the colloid surface, a long colloidal rod with planar boundary condition adopts an equilibrium direction along \hat{n} (red axis) when immersed in a chiral LC. The molecular orthogonal frame (\hat{n} , $\hat{\chi}$, $\hat{\tau}$), which is marked in each phase contrast micrograph, is robustly controlled by substrates with planar-anchoring forces (Methods). The average orientations of the colloidal rod in each vertical focal plane, again, align consistently with the designed background helix, which rotates along the sample depth [Fig. 4(a)]. The twisting rate, corresponding to the cholesteric pitch, is found by plotting the rod orientation (which is along \hat{n}) against the depth along the helical $\hat{\chi}$ axis [Fig. 4(b)] and by performing a linear fit. The orientational distribution of the thin rod is then projected and visualized within the corotating molecular frame. The fluctuations are optically observed from depth slice planes (along the angle δ , from \hat{n} towards $\hat{\tau}$) as demonstrated in Fig. 4(c) with empirical data points fitted. Due to restrictions on the vertical resolution of the phase contrast microscopy, we calculate the orientational distribution of rod angles η (from \hat{n} towards $\hat{\chi}$) based on the theory outlined in the sections below and in Ref. [29]. The model also provides adequate fitting expressions for the distribution curves shown. The orientational fluctuations along the two distinct directions are weakly asymmetric, demonstrating a clear biaxial signature imparted by the chiral molecular host.

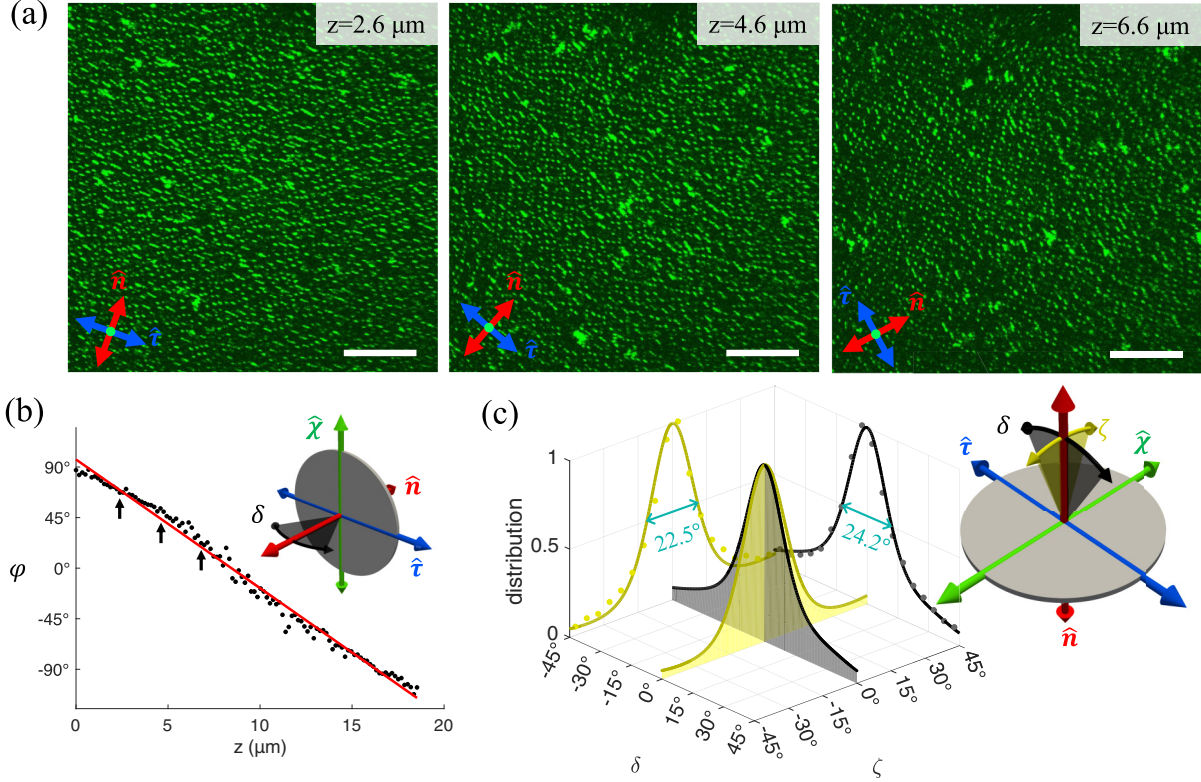


FIG. 3. (a) Depth-resolved luminescence confocal micrographs of homeotropic disks dispersed in a chiral LC host. The image slice planes are perpendicular to $\hat{\chi}$, showing the side view of the thin colloidal disks orientating along \hat{n} . Sample depths z and corresponding cholesteric directors \hat{n} and $\hat{\tau}$ are marked in each optical slice. (b) Average azimuthal orientation φ of disks in each z slice (dots) and their linear fit (red line), showing helixlike alignment of disks along the depth z . Dots corresponding to the slices in (a) are marked using arrows. The 360° -rotation period, identified with cholesteric pitch, is found to be $p \approx 30 \mu\text{m}$. The inset defines the fluctuation angle $\delta = \varphi - 360^\circ/(pz)$. (c) Orientational fluctuations of the disks visualized in the corotating molecular frame (\hat{n} , $\hat{\chi}$, $\hat{\tau}$). Deviation angles δ (from \hat{n} towards $\hat{\tau}$) and ζ (from \hat{n} towards $\hat{\chi}$) are defined in the inset. Dots represent experimental data with fitting curves derived from theory detailed in Sec. III D. Scale bars are $30 \mu\text{m}$. Similar experimental data have been reported in a previous work [29].

The symmetry-breaking behavior observed for rods with perpendicular boundary conditions is more pronounced compared to the planar case. For homeotropic surface anchoring, the rods align towards the $\hat{\tau}$ axis under thermal equilibrium [Fig. 5(a)]. Using a similar approach, we measured the azimuthal angle φ of the long rod axis in each z slice [Fig. 5(b)] and converted these data to a 3D distribution within the molecular frame [Fig. 5(c)]. We find that the orientation probability distribution is much more strongly biaxial than for rods with a planar boundary. Furthermore, compared to previously reported results for homeotropic rods [29], a larger energy cost develops for the longer colloidal rods to fluctuate away from the energetically ideal configuration along $\hat{\tau}$ (the peak width in γ being 16.6° compared to 28.1° in Ref. [29]) due to the larger surface area of the longer particle, to which the surface energy is proportional. The orientational distributions of homeotropic rods behave dramatically differently from the nonchiral limit, in which case a degeneracy of alignment along the $\hat{\chi}$ and $\hat{\tau}$ axes is expected and the distribution along η should be uniform leading to a uniaxial orientational symmetry. Instead, we find an exceptionally strong energetic hindrance for rods deviating along η towards the helical axis $\hat{\chi}$ [Fig. 5(c)]. The symmetry of the hybrid LC system is thus strongly biaxial as illustrated

by the distinctly different peak widths of the orientational probability distributions. We will demonstrate that in the case of homeotropic anchoring the rod orientation distributions cannot be rationalized from surface-anchoring effects alone, but require consideration of the elastic distortions generated in the bulk of the molecular host. This is addressed in detail in the following sections using a comprehensive analytical model.

D. Analysis of the surface-anchoring free energy of thin colloids immersed in a cholesteric host

In order to aid the interpretation of our experimental observations with a simple analytical model, we consider a low-molecular-weight chiral liquid crystal with a director field $\hat{n}(z)$ twisted along the $\hat{\chi}$ axis of a Cartesian laboratory frame that we denote by the normalized unit vectors $(\hat{x}, \hat{y}, \hat{z})$ where \hat{z} coincides with the helical axis $\hat{\chi}$ in Fig. 1. The helical director field of a cholesteric, denoted by subscript “ h ,” may be parametrized as follows

$$\hat{n}_h(z) = \hat{x} \cos qz + \hat{y} \sin qz, \quad (4)$$

in terms of the cholesteric pitch $p = 2\pi/q$ and handedness $q < 0$ that we assume left-handed in agreement with

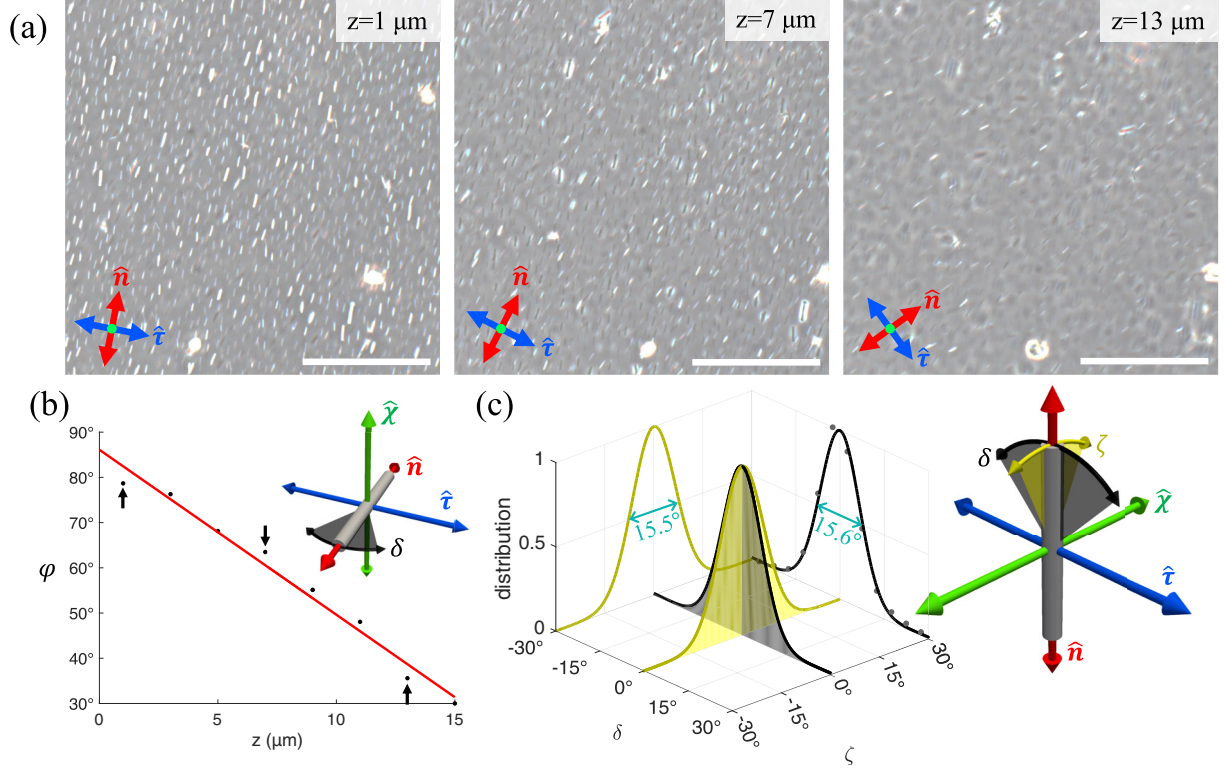


FIG. 4. (a) Phase contrast micrographs showing depth-dependent slices of planar rods dispersed in chiral molecular 5CB. (b) Average rod orientation in each z slice (dots) and linear fit (red line). The cholesteric pitch is $p \approx 100 \mu\text{m}$. (c) Azimuthal and polar orientational distribution of the rods preferentially pointing along \hat{n} (red axis). Experimental data for δ distribution are marked by black dots with a fitting curve provided by the theoretical model (see Sec. III D). Scale bars denote $30 \mu\text{m}$.

experimental reality without loss of generality. Next, we immerse an infinitely thin cylindrical disk with aspect ratio $D_c/L_c \rightarrow \infty$ into a cholesteric host. The main symmetry axis of the colloidal disk is the surface normal parametrized within a Cartesian laboratory frame $\{\hat{x}, \hat{y}, \hat{z}\}$ via $\hat{u} = \hat{x} \sin \theta \sin \varphi + \hat{y} \sin \theta \cos \varphi + \hat{z} \cos \theta$ in terms of a polar θ and azimuthal angle φ with respect to the helical axis $\hat{z} = \hat{\chi}$. The presence of the colloid will generate elastic distortions of the uniform director field $\hat{n}_h(\mathbf{r})$ due to the specific anchoring of the molecules at the colloidal surface, quantified by the surface-anchoring strength $W_0 > 0$ (units of energy per surface area). The extent of the elastic distortions around the colloid surface depends on the surface extrapolation length $\ell_s = K/W_0$ where K denotes the average elastic constant of the thermotropic liquid crystal [48]. In our analysis, we first focus on the regime of infinitely large surface extrapolation length ($\ell_s \rightarrow \infty$), in which case the elastic distortions around the immersed colloid are absent. For finite ℓ_s , such as in the experimental situation, elastic distortions are weak but non-negligible and will be discussed in Sec. III F. The reader is referred to Ref. [29] and the Appendix for the technical details of these calculations. We start by assuming the molecular director field \hat{n} to remain completely undistorted by the presence of the colloids so that there are no nematic forces within the bulk of the host. Then the only forces at play are the anchoring of the molecular host at the surface of the colloid. The corresponding free energy can be obtained from the Rapini-Papoular model for Eq. (4) and integrating over the colloid surface denoted by S

[49,50]

$$F_s = -\frac{1}{2} W_0 \oint dS [\hat{n}_h \cdot \hat{v}(S)]^2, \quad (5)$$

where \hat{v} represents a unit vector normal to the colloid surface in the case of homeotropic (H) anchoring and tangential to the surface if the anchoring is planar (P). Let us denote its normal by \hat{u} and ignore anchoring at the rim. We further define two unit vectors $\hat{e}_{1,2}$ orthogonal to the disk normal vector \hat{u} . The two principal anchoring scenarios, H and P, are expressed as follows

$$\hat{v} = \begin{cases} \hat{u}, & H \\ \hat{e}_1 \cos \xi + \hat{e}_2 \sin \xi, & P. \end{cases} \quad (6)$$

The angle $0 < \xi < 2\pi$ must be chosen randomly in the case when planar anchoring is degenerate across all directions on the disk surface, which is the case in most experimental situations. Using suitable parametrizations of the disk surface, the integral can be worked out in closed form. Details of the computations are given elsewhere in [29]. The following generic expression is obtained

$$F_{s,\text{disk}} = -\frac{\pi}{4} W_0 D_c^2 \left(w_1 + w_2 \cos(2\delta) \frac{J_1(qD_c |\sin \theta|)}{qD_c |\sin \theta|} \right) \quad (7)$$

with $J_1(x)$ a Bessel function of the first kind, $\delta = \varphi - qz$ the azimuthal angle with respect to the local cholesteric director,

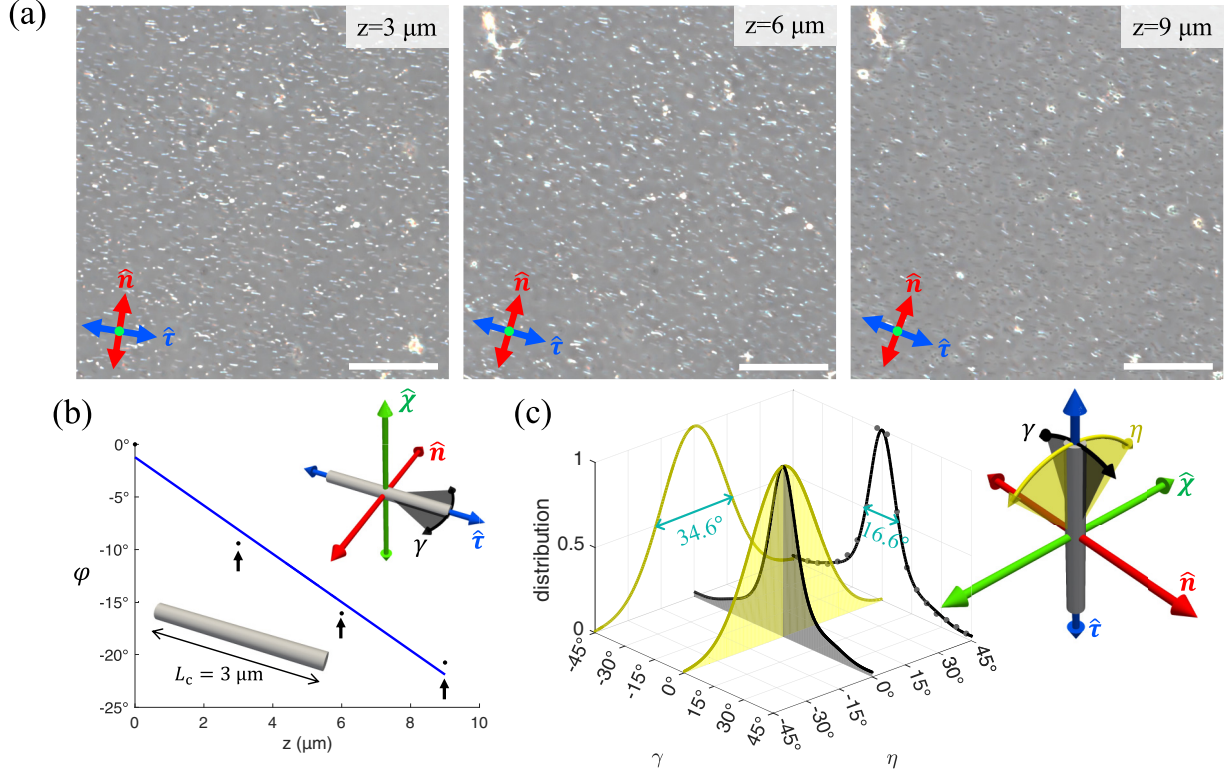


FIG. 5. (a) Phase contrast micrographs of a dispersion of homeotropically anchored rods immersed in a chiral LC taken at different focal depths as labeled on each image. (b) Average orientation of the long axis of each rod ϕ in each depth z slice (dots) and its linear fit (blue line). Cholesteric pitch $p \approx 150 \mu\text{m}$ and average rod length $L_c = 3 \mu\text{m}$. (c) Orientational fluctuations of the rods measured within the LC molecular frame (inset) with average direction $\hat{\tau}$ (blue axis). Black dots denote the experimental distribution of γ while the yellow curve is the corresponding prediction from the theoretical model (see Sec. III D). Scale bars denote $30 \mu\text{m}$.

and coefficients

$$w_1 = \begin{cases} \frac{1}{2} \sin^2 \theta, & H \\ \frac{1}{8}[3 + \cos(2\theta)], & P, \end{cases} \quad (8)$$

and

$$w_2 = \begin{cases} \sin^2 \theta, & H \\ -\frac{1}{2} \sin^2 \theta, & P. \end{cases} \quad (9)$$

The surface-anchoring strength of disks is expressed in dimensionless form by $\bar{W} = \beta W_0 D_c^2$ with $\beta^{-1} = k_B T$ the thermal energy in terms of temperature T and Boltzmann's constant k_B . Taking disks with diameter $D_c \approx 2 \mu\text{m}$ and $W_0 \approx 10^{-6} - 10^{-5} \text{J m}^{-2}$ we find $\bar{W} \sim 10^3 - 10^4$, indicating that surface-anchoring realignment is robust against thermal fluctuations in the experimental regime. For the case of homeotropic anchoring, the surface-anchoring energy, Eq. (7), reaches a minimum at an equilibrium angle $\theta^* = \pi/2$ and $\delta^* = 0$, demonstrating preferential alignment of the disk normal along the local LC host director $\hat{\mathbf{n}}$, in agreement with experimental observation (Fig. 3).

We may repeat the previous analysis to describe the case of a thin colloidal rod with $L_c/D_c \rightarrow \infty$ by neglecting small contributions associated with the ends of the cylinder so we only consider anchoring forces at the cylindrical surface of magnitude following the principal contour along $\hat{\mathbf{u}}$. In order to describe various anchoring situations, we define two unit

vectors $\hat{\mathbf{e}}_{1,2}$ orthogonal to $\hat{\mathbf{u}}$ and parametrize

$$\hat{\mathbf{v}} = \begin{cases} \hat{\mathbf{e}}_1 \cos \phi + \hat{\mathbf{e}}_2 \sin \phi, & H \\ -\hat{\mathbf{e}}_1 \sin \phi \cos \xi + \hat{\mathbf{e}}_2 \cos \phi \cos \xi + \hat{\mathbf{u}} \sin \xi, & \text{DP} \\ \hat{\mathbf{u}}, & \text{SP}. \end{cases} \quad (10)$$

In the case of homeotropic (H) anchoring, the molecular director favors perpendicular alignment at the cylindrical surface, whereas for a simple planar (SP) surface anchoring, the direction along the main rod is favored. For completeness, we also include the more general case of a degenerate planar (DP) surface, where all anchoring directions perpendicular to the local surface normal are equally probable. In order to account for all possible rod orientations with respect to the molecular field, the angle ξ can take values between 0 and π . We obtain the following generic expression

$$F_{s,\text{rod}} = -\frac{\pi}{8} L_c D_c W_0 \left(w_1 + w_2 \cos(2\delta) \frac{\sin(q L_c \cos \theta)}{q L_c} \right). \quad (11)$$

Similar to the previous case of disks, w_1 and w_2 are angle-dependent coefficients that depend on the particular anchoring situation

$$w_1 = \begin{cases} (1 + \cos^2 \theta) & H \\ \frac{1}{2}(3 - \cos^2 \theta) & \text{DP} \\ 2 \sin^2 \theta & \text{SP} \end{cases} \quad (12)$$

and

$$w_2 = \begin{cases} -\sin\theta \tan\theta, & H \\ \frac{1}{2}\sin\theta \tan\theta, & DP \\ 2\sin\theta \tan\theta, & SP, \end{cases} \quad (13)$$

in terms of the polar θ and azimuthal rod angle φ with respect to the helical axis along the $\hat{\chi}$ direction.

For the H case the free energy is minimal at an equilibrium angle $\theta^* = 0$ (with the azimuthal angle φ randomly distributed), which corresponds to the rod being aligned along the $\hat{\chi}$ direction. However, there is a second, degenerate minimum at $\theta^* = \pi/2$ and $\delta^* = \pi/2$, that describes a rod pointing along the $\hat{\tau}$ axis. The minimum surface-anchoring energy is $F_s = -(\pi/4)L_c D_c W_0$ for both cases. The energy barrier between the two minima is only about $1k_B T$ per rod so thermal fluctuations should easily make the colloids switch from one state to the other while staying perpendicular to $\hat{\mathbf{n}}$. In Sec. III F we argue that this degeneracy is lifted by the elastic distortions around the rod, which are commensurate to the twisting of the chiral host in the one but remain untwisted in the other [29]. For both SP and DP anchoring, we only find a single minimum at $\theta^* = \pi/2$ and $\delta^* = 0$, i.e., the rod preferentially aligns along the revolving local nematic director $\hat{\mathbf{n}}$ as observed in experiment (see Fig. 4).

E. Biaxial symmetry breaking of the colloid orientational probability distribution

Balancing the surface-anchoring free energy against the orientational entropy of the individual colloids, we establish their orientational probability through the Boltzmann distribution

$$f(\hat{\mathbf{u}}) \propto \exp(-\beta F_s). \quad (14)$$

It is straightforward to infer from Eqs. (7) and (11) that the polar and azimuthal angles are strongly coupled in general. Taking, for instance, Eq. (7) for homeotropic disks, reexpressing the angular components in terms of the projections of the disk normal $\hat{\mathbf{u}}$ onto the local tripod ($\hat{\chi}$, $\hat{\tau}$, $\hat{\mathbf{n}}$) comoving along the helical pitch direction (Fig. 1), and Taylor expanding the Bessel function up to leading order for weak chirality $qD_c \ll 1$, we obtain a more insightful expression

$$F_{s,\text{disk}} \approx -\frac{\pi}{4}W_0 D_c^2 \times \left[(\hat{\mathbf{u}} \cdot \hat{\mathbf{n}})^2 - \frac{(qD_c)^2}{16} [(\hat{\mathbf{u}} \cdot \hat{\tau})^2 + (\hat{\mathbf{u}} \cdot \hat{\mathbf{n}})^2] \right]. \quad (15)$$

This demonstrates that the distribution of colloid orientations around the principal alignment direction $\hat{\mathbf{n}}$ is strictly uniaxial around $\hat{\mathbf{n}}$ for achiral hosts but is rendered *biaxial* for any nonzero chiral twist $|q|D_c > 0$ with the $\hat{\tau}$ axis taking the role as a secondary axis of alignment. The biaxial symmetry breaking featured in the orientational probability about the main direction of alignment is clearly reflected in all three cases we considered in our experiments: homeotropic disks [29], planar rods [Fig. 4(c)], and homeotropic rods [Fig. 5(c)]. The response of the biaxial order parameter with increasing chiral strength is, however, different for each of these cases. This will be further discussed in Sec. IV. The case of homeotropic

rods constitutes a more extreme case of biaxial symmetry breaking that is broken by the elastic distortions enveloping the rod, as we will discuss next.

F. Role of elastic deformations surrounding the colloid surface

So far we have ignored the role of weak elastic deformations of the host director ($\ell_s = K/W_0 \rightarrow \infty$) by assuming colloidal reorientation to be dominated entirely by surface-anchoring torques acting on the immersed particles. The experimental reality, however, is that the surface-anchoring extrapolation length is large but finite ($\ell_s \approx 600 \text{ nm} \gg D_c$). The observations compiled in Fig. 5 point at a scenario where rods orient preferentially along the τ direction, rather than the helical axis ($\hat{\chi}$) as predicted from minimizing the bare Rapini-Papoular surface-anchoring energy. In Ref. [29] we have demonstrated that the discrepancy is due to a twisting of the surface disclination that runs along the rod contour, which costs elastic energy. No such twisting is required if the rod points along $\hat{\tau}$. The cost in elastic energy between the twisted ($\hat{\chi}$) and untwisted ($\hat{\tau}$) alignment directions is independent of the surface-anchoring extrapolation length ℓ_s and increases logarithmically with system size ℓ_{max} [29]

$$\Delta F_{\text{twist}}^{(\text{el})} \sim \frac{\pi}{12} (qL_c)^2 L_c \Delta K \ln \left(\frac{2\ell_{\text{max}}}{D_c} \right). \quad (16)$$

Taking $\ell_{\text{max}} = L_c$ as the typical size cutoff, and a splay-bend elastic anisotropy $\Delta K = 4 \text{ pN}$, we find that $\Delta F_{\text{twist}} \sim O(10^2 k_B T)$. The corresponding change in the Rapini-Papoular surface-anchoring free energy associated with the director distortions is estimated as

$$\Delta F_{\text{twist}}^{(s)} \sim -\frac{\pi W_0 L_c D_c}{92} \frac{D_c}{\ell_s} (qL_c)^2, \quad (17)$$

which is only a fraction of the thermal energy so that the total distortion-induced free-energy change can be safely estimated from $\Delta F_{\text{twist}} \approx \Delta F_{\text{twist}}^{(\text{el})}$.

By including the twisted disclination effect, we revisit the realigning potential acting on a rod immersed in a cholesteric host. The total external potential is given by the bare Rapini-Papoular contributions for the undistorted host director plus the free-energy contributions from elastic distortions

$$F_{s,\text{tot}} = F_{s,\text{rod}} + \Delta F_{\text{dist}}. \quad (18)$$

Since the distortion term cannot be resolved for any rod orientation but only for cases when the rod is aligned along either of the directions of the local frame ($\hat{\mathbf{n}}$, $\hat{\tau}$, $\hat{\chi}$) of the helical LC host frame, we propose the following interpolation form

$$\Delta F_{\text{dist}}(\eta, \gamma) \sim \Delta F_{\text{twist}} \sin^2 \eta + \Delta F_{\text{tilt}} \cos^2 \eta \sin^2 \gamma, \quad (19)$$

in terms of the two angles $\eta = \theta - \frac{\pi}{2}$ and $\gamma = \delta - \frac{\pi}{2}$ represented in Figs. 5(c) and 5(f) and key elastic contributions; $\Delta F_{\text{twist}} = F(\hat{\mathbf{u}} \parallel \hat{\chi}) - F(\hat{\mathbf{u}} \parallel \hat{\tau})$ [Eq. (16)] and $\Delta F_{\text{tilt}} = F(\hat{\mathbf{u}} \parallel \hat{\mathbf{n}}) - F(\hat{\mathbf{u}} \parallel \hat{\tau})$ associated with tilting the rod away from the τ axis towards the $\hat{\mathbf{n}}$ direction. An expression for the energy cost associated with tilting has been obtained

in Ref. [29]

$$\Delta F_{\text{tilt}} \sim W_0 L_c D_c \left(1 - \frac{49\zeta(3)}{8\pi^3 \ell_s} \right) \gamma^2 + O(\gamma^2/\ell_s^2) \quad (20)$$

with $\zeta(3) \approx 1.2$ a constant from the Riemann-Zeta function $\zeta(x)$. While F_{twist} amounts to a few hundreds of $k_B T$, the elastic distortions due to tilting turn out smaller than the thermal energy ($\Delta F_{\text{tilt}} < k_B T$) and may, in fact, be neglected altogether for the weak anchoring regime the rods operate in. The total energy $F_{s,\text{tot}}$ experienced by a homeotropically anchored rod is minimal (zero) when the rods align along the $\hat{\tau}$ directions ($\theta^* = \pi/2$ and $\delta^* = \pi/2$) as observed in our experiment (Fig. 5). In fact, the energy contribution associated with the twisted disclination can be estimated from the width of the distributions depicted in panel (c). For small angles η the Boltzmann factor of Eq. (19) translates into a simple Gaussian distribution

$$f(\eta) \propto \exp(-\Delta F_{\text{twist}} \eta^2), \quad (21)$$

and we identify a standard Gaussian FWHM = $2.355/\sqrt{2\Delta F_{\text{twist}}}$. This subsequently gives $\Delta F_{\text{twist}} \approx 33k_B T$ for the long rods with $L_c = 3 \mu\text{m}$ suggesting that the thermal motion of the rods is assuredly insufficient to overcome the energy barrier between the τ and χ alignment directions. The values are in qualitative agreement with the prediction from our analytical model, Eq. (16), where $\Delta F_{\text{twist}} \propto L_c^3$ suggests that the elastic energy cost of orientating the rods from the $\hat{\tau}$ to $\hat{\chi}$ directions is indeed quite sensitive to the colloidal rod length L_c . The actual values from Eq. (16), however, should be considered as an upper bound for ΔF_{twist} mainly because in our model the local nematic order parameter S_m of the host is constrained at its far-field bulk value and is not allowed to relax in regions where director distortions are the largest, as observed in our experiment and simulations.

As for homeotropic disks, similar weak deformations of the director are incurred near the colloid surface [Figs. 1(b) and 1(c)] [29]. As expected, the topology of these deformations is strictly chiral [29]. The elastic distortions around the disk have been analyzed in the Appendix but turn out to be rather immaterial for the realignment potential of the disks which remains dominated by the Rapini-Papoular surface-anchoring free energy given by Eq. (7) (Fig. 6), so that in good approximation we have $F_{s,\text{tot}} \approx F_{s,\text{disk}}$. Analogously for the case of rods with planar anchoring (Fig. 4), we expect an outcome similar to that of disks, namely, surface anchoring enforces the rods to align along $\hat{\mathbf{n}}$ with fluctuations away from the preferred direction being strongly penalized by unfavorable surface-anchoring conditions at the colloid surface.

G. Colloidal nematic order parameters

To connect to the conventional representation of orientational order, we define colloidal nematic order parameters that measure the principal direction of alignment of the colloids along the cholesteric helix. Taking the local molecular LC director $\hat{\mathbf{n}}$ as a reference frame, we define a colloidal uniaxial order parameter as follows

$$S_{\text{cm}} = \langle \mathcal{P}_2(\hat{\mathbf{u}} \cdot \hat{\mathbf{n}}) \rangle_f, \quad (22)$$

with $\langle \dots \rangle_f$ denoting a thermal average, and a colloidal biaxial nematic order parameter that measures the relative orientational order with respect to the principal directions orthogonal to $\hat{\mathbf{n}}_h$

$$\Delta_{\text{cm}} = \langle (\hat{\mathbf{u}} \cdot \hat{\boldsymbol{\tau}})^2 - (\hat{\mathbf{u}} \cdot \hat{\boldsymbol{\chi}})^2 \rangle_f. \quad (23)$$

Alternatively, we can probe the orientational order from the tensorial order parameter for colloids $\mathbf{Q}_c = \frac{3}{2}(\hat{\mathbf{u}} \otimes \hat{\mathbf{u}})_f - \frac{1}{2}\mathbf{I}$ which measures orientational order with respect to the principal colloidal alignment direction independently from the chosen reference frame. The corresponding uniaxial and biaxial order parameters defined within the colloidal frame are denoted by S_{cc} and Δ_{cc} , respectively. In case the colloids align along the molecular director $\hat{\mathbf{n}}$, such as a homeotropic disk (Fig. 3) or a planar rod (Fig. 4), the colloidal and molecular frames coincide and the corresponding values of order parameters are identical.

To quantify the biaxial symmetry breaking of the colloidal orientational distribution found in experiment, we determine the uniaxial S_{cm} and biaxial Δ_{cm} order parameters for both disks and rods (Table I). The uniaxial order parameter S_{cc} , as a measure of unidirectional ordering [Eq. (22)], represents the strength of orientational alignment which depends sensitively on the synthesized material and on the surface-anchoring type. Subsequently, the strict nonequivalence of the two axes orthogonal to the principle molecular alignment directions is evaluated from the biaxial order parameter Δ_{cm} [Eq. (23)], with $-1 < \Delta_{\text{cm}} < 1$. The values of S are determined to be $S_{\text{cc}} = S_{\text{cm}} = 0.66$ for homeotropic disks dispersed in chiral 5CB-based LC (Fig. 3) and $S_{\text{cc}} = S_{\text{cm}} = 0.94$ for rods with a planar boundary condition (Fig. 4). The values of Δ_{cm} are found to be 0.067 and 0.016, respectively, with the nondegeneracy among $\hat{\boldsymbol{\chi}}$ and $\hat{\boldsymbol{\tau}}$ imparting robust biaxial orientational symmetry.

When the average orientations of the two components differ, the values of the order parameters depend on the choice of reference frame. Stronger orientational fluctuations are found for the shorter rods with homeotropic anchoring (Table I) with $S_{\text{cc}} = 0.70$ and $\Delta_{\text{cc}} = 0.12$, while the longer rods in Fig. 5 exhibit a larger uniaxial order parameter $S_{\text{cc}} = 0.80$ but weaker biaxiality $\Delta_{\text{cc}} = 0.018$, at a similar level to what was measured for planar rods.

The enhanced biaxiality for homeotropic rods aligning perpendicular to the molecular director $\hat{\mathbf{n}}$ will be discussed in the following section. Calculated within the molecular reference frame, the negative values of S_{cm} and the large values of Δ_{cm} simply reflect the geometry where the colloidal director lies perpendicular to the molecular director $\hat{\mathbf{n}}$.

IV. DISCUSSION

A. Enhanced biaxial symmetry breaking at perpendicular molecular-colloidal alignment

For colloidal rods immersed in a chiral LC, the biaxial order developed at the level of the colloids is much more pronounced for rods with a homeotropic boundary condition, whose energetically favored orientation is along $\hat{\boldsymbol{\tau}}$ perpendicular to the local molecular director $\hat{\mathbf{n}}$. As a consequence, the rotational symmetry around the rotation axis $\hat{\boldsymbol{\tau}}$ is no longer continuous, with $\hat{\mathbf{n}}$ being the material axis representing the

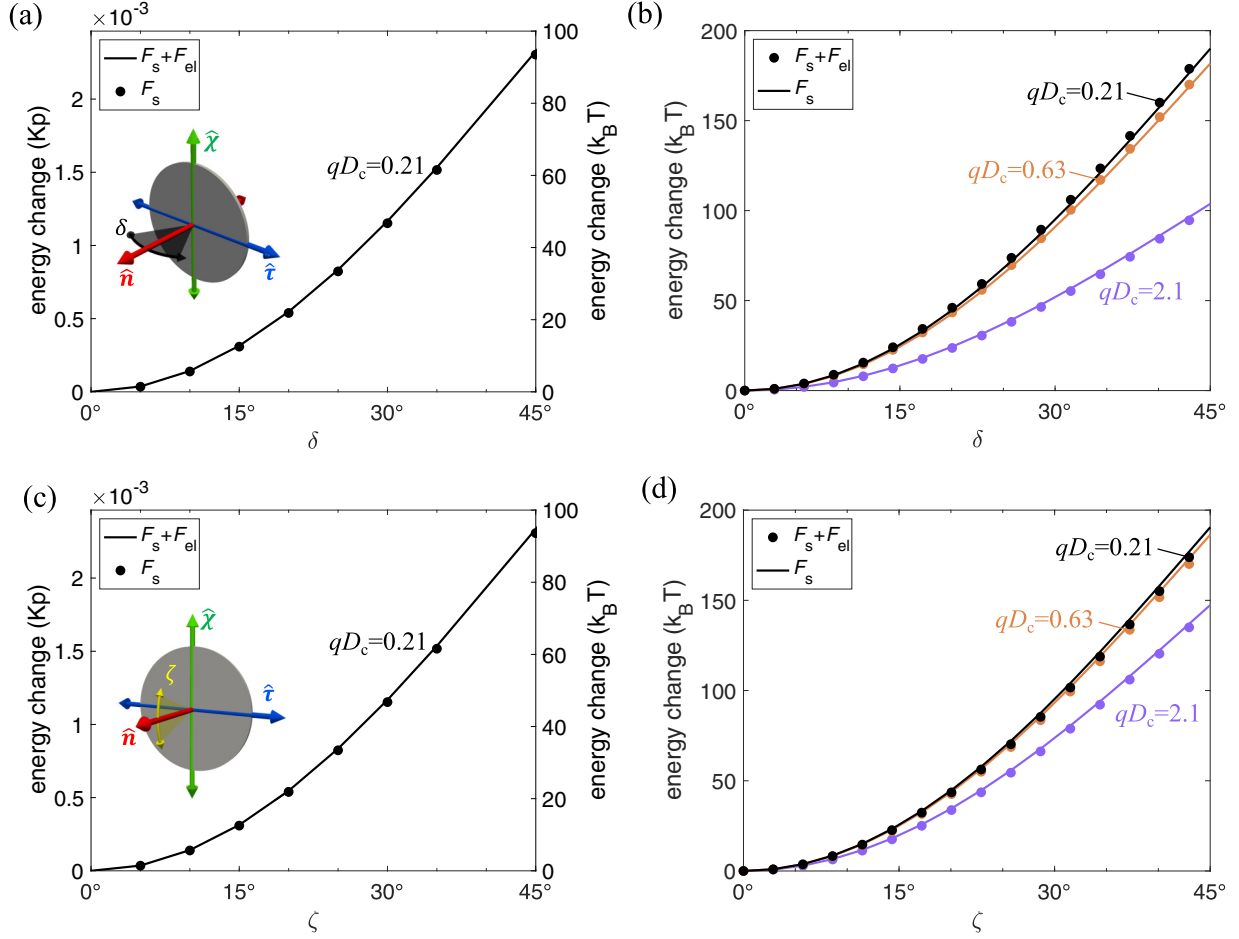


FIG. 6. (a) Molecular LC surface-anchoring energy obtained from computer simulation with (solid line) or without (dots) the elastic distortion energy. The energy is obtained using a Q-tensor description of a chiral 5CB-based LC surrounding a homeotropic disk at different angles δ defined in the inset. The left and right plot axes denote different energy units. (b) The corresponding prediction from analytical theory for different values of LC chiral strength qD_c . Solid lines correspond to the surface-anchoring energy alone, while dots include the contribution of weak elastic distortion around the colloidal disk (see Appendix). (c), (d) Numerical simulation (c) and theoretical prediction (d) of the free energy for homeotropic disks at different angles ζ (defined in the inset). Note that biaxiality is manifested by the small but unavoidable energy difference between (a), (b) and (c), (d) and is also shown in Fig. 2(c). Surface-anchoring strength $W_0 = 10^{-6} \text{ J m}^{-2}$ and cholesteric pitch $p = 30 \mu\text{m}$. Disk dimensions $L_c = 10 \text{ nm}$ and $D_c = 1 \mu\text{m}$ for all simulations and calculations. The energy zero points are chosen at $\delta = 0$ or $\zeta = 0$.

actual molecular direction and $\hat{\chi}$, in contrast, an “imaginary” one (see Fig. 5). The resulting symmetry breaking is thus much more outspoken than in the case of colloids preferentially aligning along \hat{n} . This remarkable manifestation of biaxial symmetry breaking for the case of homeotropic rods is rationalized from analytical theory which highlights the subtle role of weak but non-negligible elastic distortions enveloping each rod. These induced distortions more strongly disrupt the alignment of the surrounding molecules than for the case of rods with planar or parallel anchoring boundary conditions. The significant contribution from the elastic energy of the background molecular LC to the total free energy [Eq. (19)] affords additional control of emergent biaxiality, for instance, by tuning the elastic properties of the molecular host to further boost the intrinsic biaxiality of the hybrid LC. Likewise, disks with planar anchoring, which could be realized through appropriate surface functionalization [33], are expected to exhibit equivalent perpendicular alignment (but this time along the

helical axis $\hat{\chi}$) which would also impart strongly enhanced biaxial order in the disk orientation distribution.

B. Quadratic scaling of the biaxial order parameter with chirality

In the weak molecular chirality regime, we may characterize the leading-order contribution of chirality to colloidal biaxiality by expanding the biaxial order parameter up to the quadratic order in the inverse pitch $q = 2\pi/p$ [29]

$$\Delta_{cc} = \Delta_0(qa)^2 + O[(qa)^4], \quad (24)$$

where the length scale corresponds to the colloidal dimensions; $a = D_c$ for thin disks and $a = L_c$ for cylindrical rods. The zeroth-order term must be zero given that no intrinsic biaxiality can be expected from purely uniaxial components at zero chirality. Also, the linear term proportional to qa must vanish since the value of biaxiality should not depend

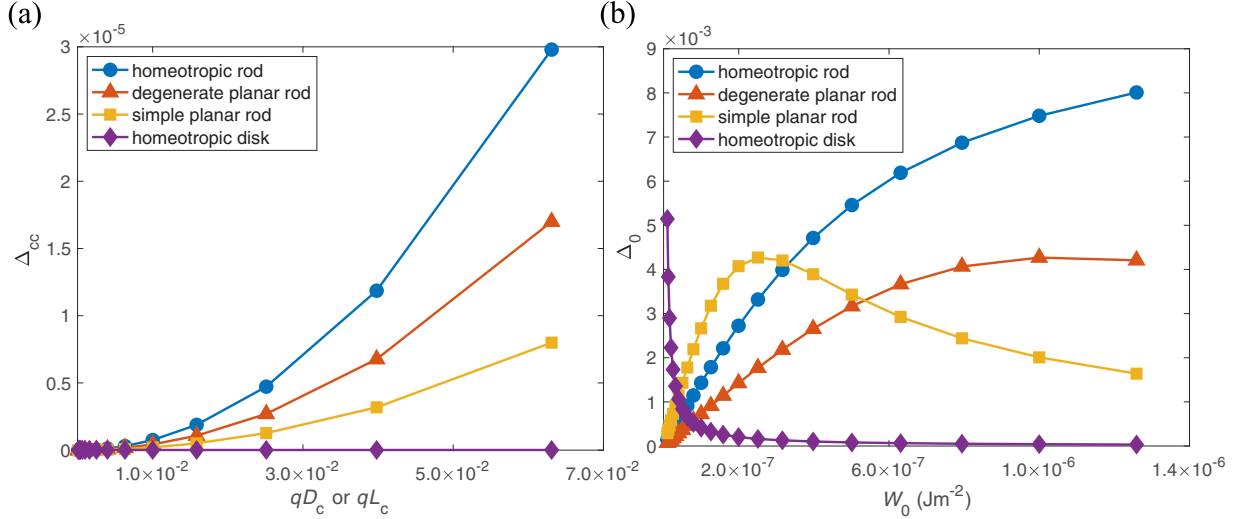


FIG. 7. (a) Quadratic scaling of the biaxial order parameter Δ_{cc} for the colloidal orientation distribution in the weak chirality regime $qa \ll 1$, with a the typical colloid size. The results are based on the Rapini-Papoular surface-anchoring energy Eqs. (5) and (14) using $W_0 = 10^{-6} \text{ J m}^{-2}$. (b) Dependence of the prefactor Δ_0 , defined by $\Delta_{cc} \sim \Delta_0(qa)^2$ on the anchoring strength based on the colloidal dimensions $L_c = 1.7 \mu\text{m}$ and $D_c = 28 \text{ nm}$ for the rods and $L_c = 20 \text{ nm}$, $D_c = 2 \mu\text{m}$ for the disks.

on the handedness of the host material. Following the results Eq. (14), Eq. (23), and the free energies for each type of colloids, we computationally verify the quadratic scaling $\Delta_{cc} \sim \Delta_0(qa)^2$ within the weak chirality approximation $qa \ll 1$ [Fig. 7(a)]. Interestingly, the quadratic scaling of biaxial order with the parameters qL_c or qD_c resembles the theoretical prediction by Priest and Lubensky for a single-component molecular LC [19], in which case L_c needs to be replaced by L_m denoting the size of the molecules. Despite the different derivations of biaxiality from component material(s), the agreement between the results from our hybrid LC system and single-compound LC reveals the underlying physical principle, namely, a close relationship between biaxial order and chirality. Most interestingly, the prefactor Δ_0 turns out to be very different for each system considered and has a distinct, nontrivial dependence on the surface-anchoring strength [Fig. 7(b)].

C. Enhanced biaxiality of the molecular host at the colloidal surface

The molecular biaxial order parameter Δ_m measures the broken uniaxial symmetry of the LC host (which in our experiment is 5CB). The Δ_m is associated to the tensorial local mean-field order parameter by [17,42]

$$\mathbf{Q}^{(m)} = S_m \left(\frac{3}{2} \hat{\mathbf{n}} \otimes \hat{\mathbf{n}} - \frac{\mathbf{I}}{2} \right) + \Delta_m \left(\frac{3}{2} \hat{\mathbf{m}} \otimes \hat{\mathbf{m}} - \frac{\mathbf{I}}{2} \right), \quad (25)$$

with the molecular director field $\hat{\mathbf{n}}$ and the biaxial director $\hat{\mathbf{m}}$ orthogonal to each other. Here, S_m is the scalar order parameter measuring the unidirectionality of $\hat{\mathbf{n}}$, with $S_m \geq \Delta_m \geq 0$. Accordingly, in the numerical computation, the order parameters are determined by the diagonalization of the \mathbf{Q} tensor

$$\Delta_m = \frac{2}{3}(\lambda_2 - \lambda_3), \quad S_m = \lambda_1 + \Delta_m/2, \quad (26)$$

where $\lambda_1 > \lambda_2 > \lambda_3$ are the eigenvalues of $\mathbf{Q}^{(m)}$. The directors $\hat{\mathbf{n}}$ and $\hat{\mathbf{m}}$ are then found by calculating the eigenvectors corresponding to λ_1 and λ_2 , respectively. Since eigenvalues

are interpreted as the “directionalities” along each orientation (eigenvector), the calculation of Δ_m in Eq. (26) corresponds exactly to finding the inequivalence of the two minor axes ($\hat{\mathbf{m}}$ and $\hat{\mathbf{n}} \times \hat{\mathbf{m}}$), and the value of biaxiality is a measure of the broken rotational symmetry along $\hat{\mathbf{n}}$, analogous to the colloidal orientation distributions illustrated above. Using numerical modeling based on the Q-tensor representation of the LC order parameters, we find Δ_m at a far-field helical background to be of the order of 10^{-7} , which is precisely the value predicted using $\Delta_m \sim (qL_m)^2$ with the size of a 5CB molecule being in the nanometer range $L_m = 2 \text{ nm}$ [19], showing the intrinsic biaxial order in the molecular chiral liquid crystal.

Interestingly, we also discover that Δ_m greatly increases from 10^{-7} in the far-field limit to 10^{-4} or even 10^{-3} near the colloidal surfaces (Fig. 8), being especially prominent at regions where the surface-anchoring force favors a distinct molecular director alignment from the helical far field, leading to increased surface free energy, Eq. (2). The enhanced biaxiality induced by the colloidal particles is qualitatively interpreted as the mismatch of two axes: the particle surface-anchoring orientation $\hat{\mathbf{v}}$ and the background helical aligning direction $\hat{\mathbf{n}}_h$. As a quantification of the broken uniaxial rotation symmetry of $\hat{\mathbf{n}}$, higher values of Δ_m can be found at particle surfaces with a greater discrepancy in the two orientations, with maximum Δ_m located at regions where the surface normal director is perpendicular to the background far field (Fig. 8). Furthermore, within LC regions with a Δ_m dominated by the particle surface and far exceeding the background value 10^{-7} , the biaxial director $\hat{\mathbf{m}}$ is found to coincide with the perpendicular component of the surface-anchoring director to the nematic director, $\hat{\mathbf{m}} = \hat{\mathbf{v}} - (\hat{\mathbf{v}} \cdot \hat{\mathbf{n}})\hat{\mathbf{n}}$, confirming the idea that the colloidal surface induces molecular biaxial order by introducing an energy landscape for $\hat{\mathbf{n}}$ beyond uniaxial symmetry.

In case of no host chirality, biaxial order stabilized by correlations between colloidal particles immersed in nematic

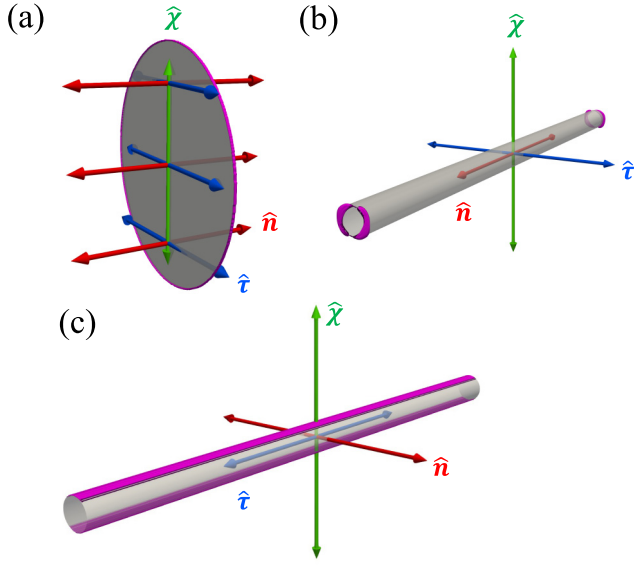


FIG. 8. (a)–(c) Contours of molecular biaxiality (magenta) around the colloids (gray) marking the regions with Δ_m larger than 10^{-3} (a) and 10^{-4} (b),(c), respectively. The orthogonal frame defining the molecular axes is colored as in Fig. 1. Homeotropic anchoring condition is used for (a) and (c) and planar anchoring for (b). Surface-anchoring strength $W_0 = 10^{-6} \text{ J m}^{-2}$ and LC helical pitch $p = 30 \mu\text{m}$ are used for all simulations.

5CB was reported in [18]. Furthermore, compared to pure molecular LCs without colloids, the frustrated alignment of $\hat{\mathbf{n}}$ induced by the presence of colloidal particles also leads to a reduced bulk nematic order parameter S_m and the formation of defects in cases with strong surface anchoring. In our systems, though, we expect the two independent contributions to the “biaxialization” of uniaxial 5CB liquid crystal—the introduction of chiral dopant and of surface-anchored colloidal particles—to have negligible effects on the free energies in our analytical model, which is evident by the relatively small induced values of $\Delta_m \ll S_m$ and has been confirmed by the numerical modeling using a tensorial order parameter $\mathbf{Q}^{(m)}$.

D. Biaxial interpretation of field configurations in chiral liquid crystals

As suggested in the section above, the intrinsic biaxiality of a chiral nematic LC allows us to define local biaxial directors even in the absence of colloidal particles. The molecular biaxial order persists, $\Delta_m \sim (qL_m)^2$, as long as the chirality q , or the helicity in the director alignment, is nonvanishing. To accurately account for this unavoidable biaxiality, we modify and expand the calculation in Refs. [51,52] for uniaxial chiral nematics, in which the chirality-associated directors ($\hat{\mathbf{n}}, \hat{\chi}, \hat{\tau}$) are found by diagonalizing a 3-by-3 handedness tensor \mathbf{H} defined as

$$\mathbf{H}_{ij} = \epsilon_{ikl} \hat{\mathbf{n}}_k \frac{\partial \hat{\mathbf{n}}_l}{\partial x_j}, \quad (27)$$

with summation over indices assumed. The trace $\sum_i \mathbf{H}_{ii} = -\hat{\mathbf{n}} \cdot (\nabla \times \hat{\mathbf{n}})$ gives the helicity of the LC director alignment

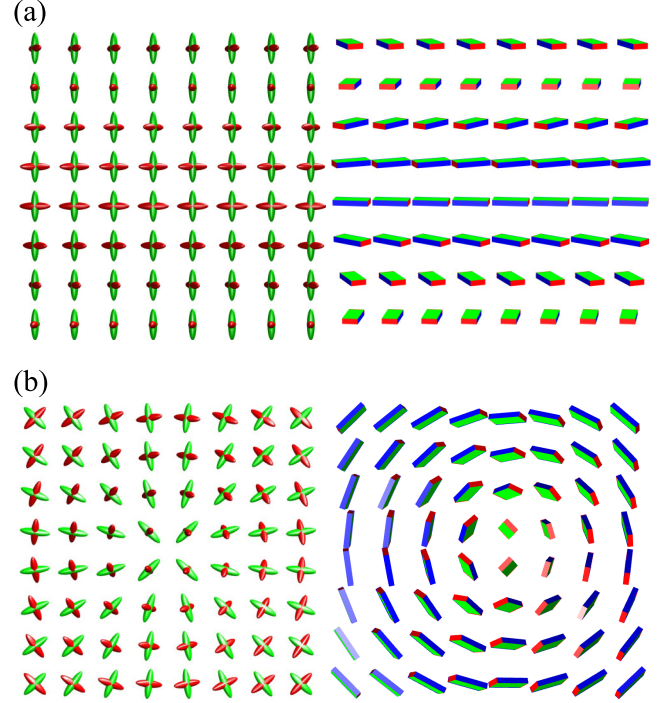


FIG. 9. (a) Director profiles simulated inside a solitonic Bloch-wall-like structure resembling a helical twist. Treated as in a uniaxial LC, $\hat{\mathbf{n}}$ (red) and $\hat{\chi}$ (green) are calculated using a chirality tensor [52] and visualized as ellipsoids (left). The directors simulated instead by a biaxial Q-tensor-based approach are visualized using bricks (right), with red, blue, and green faces, respectively, corresponding to principal $\hat{\mathbf{n}}$, biaxial $\hat{\mathbf{m}}$, and the third $\hat{\mathbf{n}} \times \hat{\mathbf{m}}$ orthogonal axes [53]. (b) Numerical simulations of molecular $\hat{\mathbf{n}}$ and helical $\hat{\chi}$ axes in a twisted defect structure using chirality-based (left) and biaxiality-based (right) approaches.

field. Considering the intrinsic biaxial order in chiral LCs, we can similarly construct the handedness tensor using the molecular tensorial order parameter $\mathbf{Q}^{(m)}$

$$\mathbf{H}_{ij} = \frac{4}{9S_m^2} \epsilon_{ikl} \mathbf{Q}_{kn}^{(m)} \frac{\partial \mathbf{Q}_{ln}^{(m)}}{\partial x_j}. \quad (28)$$

The uniaxial definition, Eq. (27), can be recovered by expanding the equation using Eq. (25) with $\Delta_m = 0$. Note that the trace of the handedness tensor again represents the helicity and is identical to the chiral part of elastic free energy [the L_4 term in Eq. (1)]. Strikingly, in our numerical simulation we discovered that the helical director field $\hat{\chi}$, which is computed as the eigenvector corresponding to the eigenvalue with the largest absolute value, closely matches the directors calculated by diagonalizing $\mathbf{Q}^{(m)}$: $\hat{\chi} = \hat{\mathbf{m}}$ (Fig. 9), which also immediately suggests $\hat{\tau} = \hat{\mathbf{n}} \times \hat{\mathbf{m}}$. (Note that all directors are head-tail symmetric.) The excellent overlap of the two orthogonal frames, ($\hat{\mathbf{n}}, \hat{\chi}, \hat{\tau}$) originating from chirality and ($\hat{\mathbf{n}}, \hat{\mathbf{m}}, \hat{\mathbf{n}} \times \hat{\mathbf{m}}$) representing biaxiality, directly demonstrates the biaxial feature in chiral nematic LCs. The energy minimizing of $\mathbf{Q}^{(m)}$ automatically incorporates these symmetries once all degrees of freedom beyond those for pure uniaxial nematics are allowed for. Consequently, one can straightforwardly identify chirality through the concomitant biaxial properties using

$q \sim \sqrt{\Delta_m}/a$ and $\hat{\chi} = \hat{\mathbf{n}}$ instead of investigating the helical twisting and spatial derivatives of the LC directors. These values are well defined from the biaxiality calculation even inside LC defects where the uniaxial order parameter S_m is reduced compared to the bulk value.

Therefore, with the chirality-driven biaxial symmetry taken into account, one can naturally analyze structures within a chiral LC using considerations similar to those derived for biaxial nematics (Fig. 9). Since the theory describing the topological classification of defects and solitons in biaxial nematics, which has an order parameter space $SO(3)/D_2$, is distinct from those emerging in a uniaxial LC with an S^2/\mathbb{Z}_2 counterpart [3,31,54–56], the biaxial symmetry in a chiral LC offers an alternative interpretation of topological objects in cholesterics differing from their more conventional description. For example, a helical configuration resembling a Bloch wall can be found across our experiments. By identifying the $\hat{\chi}$ director field within, which is uniformly aligned, we can visualize the configuration as a one-dimensional soliton formed in bricklike LCs with matching director fields (Fig. 9) with a uniform $\hat{\chi}$ field and helical twisting in the $\hat{\mathbf{n}}$ and $\hat{\mathbf{t}}$ fields. Furthermore, unlike uniaxial LCs with a single director field, biaxial systems with three orthogonal director fields cannot accommodate a fully nonsingular solitonic structure such as 2D translationally invariant fully nonsingular objects, implied by $\pi_2[SO(3)/D_2] = 0$ [3,54]. As shown in Fig. 9(b), a meronlike arrangement of directors is a nonsingular soliton embedded in the molecular director $\hat{\mathbf{n}}$. The meron, or half-skyrmion structure, has been constructed as a 2D soliton composed of a single director or vector with the absence of singularity [5,57,58]. The structure becomes, however, a singular defect in a biaxial system, as demonstrated by the emergence of singularities found at the center in the $\hat{\chi}$ and $\hat{\mathbf{t}}$ director fields orthogonal to the material director field. Similarly, 3D topological solitons, fingers, and other nonsingular structures in cholesterics can be viewed as defect lines and loops in a biaxial system by thoroughly analyzing all three directors as well [3,59]. In addition, some phenomena of the topological defects and soliton structures in a system of chiral nematics, including non-Abelian disclinations and their entanglement behaviors, can be elucidated only from the perspective of biaxial nematics' topological descriptions that are distinct from uniaxial nematics' topology [3,31,60,61]. With the biaxial directors defined and simulated in consistency with the chiral description, the biaxial features of chiral nematics, including their topological defects, solitons, and frustrated structures, can be easily and naturally explored. This opens up the possibility of using molecular-colloidal chiral nematics as model systems in the exploration of non-abelian vortices, solitonic structures with low-symmetry order parameters, etc.

V. CONCLUSION AND OUTLOOK

We demonstrate that immersing uniaxial, nonchiral colloidal rods and disks into a low-molecular-weight cholesteric liquid-crystal host leads to emergent biaxial order that we identify at both colloidal and molecular levels by combining experiment with numerical simulation and analytical theory. Unlike the previously studied case of hybrid

molecular-colloidal biaxial phases [16–18], we observe multilevel biaxial symmetry breaking at ultralow colloidal content where colloid-colloid interactions are negligible. By exploring a variety of colloidal shapes and surface-anchoring symmetries, we report biaxial order emerging at three distinct levels. First, molecular director distortions develop around each colloid which, although being of marginal extent because of weak surface-anchoring conditions, display a distinct twofold signature imparted by the cholesteric host. Second, the orientational distribution of the colloids around the local cholesteric director adopts a clear biaxial signature, and the response of the corresponding biaxial order parameter depends nontrivially upon the surface-anchoring strength as well as on the ratio of the cholesteric pitch and the principal colloidal dimension (rod length or disk diameter). Finally, at the molecular scale, we demonstrate that enhanced biaxiality emerges close to the colloidal surface at levels strongly exceeding those expected for purely molecular cholesterics.

A particularly striking manifestation of biaxial symmetry breaking is encountered for thermotropic cholesterics doped with colloidal rods with homeotropic surface anchoring. Driven by a combination of surface-anchoring forces and an energy penalty incurred by twisting a weakly developed surface disclination along the rod main axis, these rods have a strong tendency to align perpendicular to both the helical axis and the local cholesteric director, thus imparting a twofold D_{2h} orientational symmetry onto the hybrid system at each point along the cholesteric helix. By means of numerical minimization of the Landau–de Gennes energy and mean-field theory based on the Rapini-Papoular surface-anchoring energy, we reveal that the multilevel expression of emergent biaxiality in our systems is essentially a single-colloid effect that already becomes manifest at ultralow colloid concentrations.

Our results pave the way towards controlled biaxial order at both colloidal and molecular levels. By harnessing the interplay of chiral and biaxial symmetries, future research efforts could be directed along the following several emergent avenues. At larger colloidal concentrations a richer phenomenology could be expected and explored due to the more prominent roles expected to be played by steric, electrostatic, or defect-mediated colloid-colloid interactions, further enriching the surface anchoring and elastic forces discussed here. Besides the emergent symmetry breaking discussed here, one could, in principle, also apply electric or magnetic fields to reconfigure either molecular or colloidal subsystems, or both, to achieve even lower externally induced symmetries of LCs, for instance, corresponding to triclinic or monoclinic point groups.

Finally, by realizing topological solitons in the molecular-colloidal hybrid system with nontrivial chirality and biaxiality, one could reveal the stability of topological structures for various low-symmetry order parameter spaces. While ferromagnetic colloidal particle dispersions have already provided insight into the possibility of the formation of solitons in polar chiral liquid crystals [62], this study could be extended to symmetries differing from nonpolar and polar uniaxial LCs, for example, by exploring multidimensional solitonic structures corresponding to the $SO(3)/D_2$ order parameter space.

ACKNOWLEDGMENTS

We acknowledge discussions with M. Bowick, T. Lee, T. C. Lubensky, B. Senyuk, M. Ravnik, and M. Tasinkevych. We are grateful to T. C. Lubensky for providing helpful suggestions and feedback on the initial versions of this article. The experimental and numerical simulations research at University of Colorado Boulder was supported by the U.S. Department of Energy, Office of Basic Energy Sciences, Division of Materials Sciences and Engineering, under contract No. DE-SC0019293 with the University of Colorado Boulder. M.T.L. and H.H.W. acknowledge financial support from the French National Research Agency (ANR) under Grant No. ANR-19-CE30-0024 “ViroLego.” I.I.S. acknowledges the support of the International Institute for Sustainability with Knotted Chiral Meta Matter at Hiroshima University in Japan during part of his sabbatical stay, as well as the hospitality of the Kavli Institute for Theoretical Physics in Santa Barbara, when he was partially working on this article. This research was also supported in part by the National Science Foundation under Grant No. NSF PHY-1748958 (I.I.S. and J.-S.W.).

APPENDIX: ELASTIC DISTORTIONS AROUND THE DISK SURFACE

Ignoring elastic distortions, we find that disks with homeotropic surface anchoring tend to orient along the local molecular director $\hat{\mathbf{n}}$, as observed in experiment. This is the optimal situation that incurs the least amount of elastic distortions, compared to the other principal directions in which cases the disk surface would experience strongly unfavorable tangential surface ordering. However, even when the disk normal is aligned along the local nematic director, there are local mismatches between the far field and preferred surface director due to the weak twisting of the host director along the helix axis $\hat{\chi}$ and when the rod normal fluctuates away from its equilibrium orientation. The elastic distortions are expected to be weak but they will become more outspoken at shorter cholesteric pitches. It is instructive to compute the extent of these distortions along the lines of our previous analysis for rods [29]. Let us consider an infinitely thin disk with its normal pointing along $\hat{\mathbf{n}}$ and rotated over an angle δ through the helix axis $\hat{\chi}$ so that the disk vector is restricted to lie in the plane perpendicular to it. We assume weak elastic distortions Φ developing in this plane. Defining a host director in the Cartesian laboratory frame $\hat{\mathbf{n}}_h = \hat{\mathbf{x}} \cos \Phi(x, y) + \hat{\mathbf{y}} \sin \Phi(x, y)$ we find, assuming elastic isotropy, that the distortions are described by the Laplace equation

$$(\partial_x^2 + \partial_y^2)\Phi = 0. \quad (\text{A1})$$

The effect of a twisting host director is accounted for through the surface-anchoring free energy

$$F_s = -\frac{W_0}{2} \oint dS \{ \hat{\mathbf{n}}_h \cdot [\mathcal{R}(qz + \delta) \cdot \hat{\mathbf{v}}(S)] \}^2, \quad (\text{A2})$$

where S parametrizes the face of the disk (as previously we ignore finite thickness effects for disks with $D_c \gg L_c$) and $\hat{\mathbf{v}} = (1, 0, 0)$ indicating homeotropic anchoring along the surface

normal. The rotation matrix reads

$$\mathcal{R}(qz + \delta) = \begin{pmatrix} \cos(qz + \delta) & -\sin(qz + \delta) & 0 \\ \sin(qz + \delta) & \cos(qz + \delta) & 0 \\ 0 & 0 & 1 \end{pmatrix}. \quad (\text{A3})$$

A key feature is that the distortions are not uniform across the disk surface but depend on the location of the surface element with respect to the helical axis. A convenient way forward is to divide the disk surface into infinitely thin strips, with each surface element on the strip being equidistant from the center of mass along the helical axis $\hat{\chi}$ thus experiencing the same degree of elastic distortions.

For notational brevity, we implicitly normalize all lengths in units of the disk diameter D_c and parametrize the disk surface in terms of $y = \frac{1}{2} \cos \alpha$ and $z = \frac{1}{2} \sin \alpha$ with $-\pi < \alpha < \pi$. Each strip then has length $L_s = \cos \alpha$, thickness $D_s = \frac{1}{2} \cos \alpha d\alpha$, and surface $ds = L_s D_s$. The surface-anchoring free energy of an arbitrary strip with surface ds and center-of-mass distance z then reads

$$F_s^{\text{strip}} = -W_0 \{ \cos [\Phi(0, y) - qz - \delta] \}^2 ds. \quad (\text{A4})$$

The boundary condition at the strip of the disk equator ($\alpha = 0$) is defined as

$$\Phi(\infty, 0) = 0$$

$$\begin{aligned} \ell_s \partial_x \Phi(0, y) &= -\frac{1}{2} \sin \{ 2[\Phi(0, y) - qz - \delta] \} \\ &\approx \frac{1}{2} \sin [2(qz + \delta)] - \cos [2(qz + \delta)] \Phi(0, y), \end{aligned} \quad (\text{A5})$$

where we take $0 < y < 1$ for convenience. The distortions should be symmetric at the edges $[\Phi(0, 0) = \Phi(0, 1)]$. The general solution of the Laplace equation (A1) is given by

$$\Phi(x, y) = \sum_{n=1}^{\infty} e^{-n\pi x} b_n \sin(n\pi y). \quad (\text{A6})$$

Applying the boundary conditions we obtain the following expression for the coefficients

$$b_n = \frac{\sin[2(qz + \delta)]}{\cos[2(qz + \delta)] - n\pi \ell_s} \left(\frac{1 - (-1)^n}{n\pi} \right). \quad (\text{A7})$$

Given that q and $-q$ do not give equivalent results, we conclude that the distortions created near the disk surface carry a distinct chiral signature imparted by the chirality of the host LC, as evidenced by the Landau–de Gennes simulations (Figs. 1 and 8). The nature of the imprint depends on the twist angle δ between the disk normal and the molecular director $\hat{\mathbf{n}}$. We further deduce that the distortions vanish at infinitely weak surface anchoring ($\ell_s \rightarrow \infty$) and in the absence of twist and tilting ($q = 0$ and $\delta = 0$), as we expect. The elastic free energy for the total disk is given by

$$\Delta F_{\text{el}} = \frac{\pi K D_c}{4} \int_{-\pi/2}^{\pi/2} d\alpha \cos \alpha \sum_n n b_n^2, \quad (\text{A8})$$

which may be evaluated as a function of the angle δ between the disk normal and the molecular director taking the surface-anchoring extrapolation length (in units of the disk diameter D_c) to be about $\ell_s \approx 3$. The change in surface-anchoring free

energy induced by the distortions follows from linearizing Eq. (A4) and integrating over all strips:

$$\Delta F_s = \frac{W_0 D_c^2}{2} \int_{-\pi/2}^{\pi/2} d\alpha \cos^2 \alpha \sin[2(qz + \delta)] \times \sum_n b_n \left(\frac{1 - (-1)^n}{n\pi} \right). \quad (\text{A9})$$

We reiterate that z depends on the angle α via $z = \frac{D_c}{2} \sin \alpha$.

We finish our analysis by considering the case where the disk normal rotates over the $\hat{\tau}$ axis by an angle ζ . This is equivalent to the situation depicted in Figs. 2(c) and 2(d). In this situation, the tilting will generate additional weak LC director distortions across the $\hat{\chi}$ direction that we denote by the angle ϵ . The spatially dependent host director now reads

$$\hat{\mathbf{n}}_i(\mathbf{r}) = \begin{pmatrix} \cos \Phi(\mathbf{r}) \cos \epsilon(\mathbf{r}) \\ \sin \Phi(\mathbf{r}) \cos \epsilon(\mathbf{r}) \\ \sin \epsilon(\mathbf{r}) \end{pmatrix}, \quad (\text{A10})$$

with $\mathbf{r} = (x, y)$. Each distortion angle obeys the Laplace equation in the $\hat{\mathbf{n}}-\hat{\tau}$ plane

$$(\partial_x^2 + \partial_y^2)\Phi = 0, \quad (\partial_x^2 + \partial_y^2)\epsilon = 0. \quad (\text{A11})$$

The surface-anchoring free energy now takes the following form

$$F_s = -\frac{W_0}{2} \oint dS \{ \hat{\mathbf{n}}_i \cdot [\mathcal{R}_\zeta \mathcal{R}(qz) \cdot \hat{\mathbf{v}}(S)] \}^2, \quad (\text{A12})$$

where the matrix \mathcal{R}_ζ describes a rotation of the disk normal over the $\hat{\tau}$ axis [cf. Fig. 2(c)]

$$\mathcal{R}_\zeta = \begin{pmatrix} \cos \zeta & 0 & \sin \zeta \\ 0 & 1 & 0 \\ -\sin \zeta & 0 & \cos \zeta \end{pmatrix}. \quad (\text{A13})$$

Analogous to the previous case, we may derive boundary conditions from linearizing F_s for weak distortions $\Phi \ll 1$ and $\epsilon \ll 1$. Plugging in the general solution [Eq. (A6)] and defining b_n as the distortion modes pertaining to $\Phi(x, y)$ and d_n as those for $\epsilon(x, y)$, we find that both distortion angles are intricately coupled, as expected

$$b_n = c_n \cos \zeta \sin(2qz), \quad d_n = c_n \sin(2\zeta) \cos^2(qz). \quad (\text{A14})$$

From these we immediately assert the most basic scenarios: both distortions vanish for a disk in an achiral host ($q = 0$) at zero tilt ($\zeta = 0$), whereas at nonzero tilt angle only $\epsilon(d_n)$ is nonzero. For a disk immersed in a chiral host ($q \neq 0$) at zero tilt ($\zeta = 0$), we recover the previous scenario with $\Phi(b_n)$ given by Eq. (A7) and $\epsilon(d_n) = 0$. Both distortion angles are expected to be nonzero in case the disk normal is tilted away from the local director of the chiral host. The common prefactor reads

$$c_n = \frac{2 \left(\frac{1 - (-1)^n}{n\pi} \right)}{1 + 2\ell_s n\pi - \cos(2\zeta) - 2 \cos^2 \zeta \cos(2qz)}. \quad (\text{A15})$$

The change in elastic free energy is a simple superposition of amplitudes

$$\Delta F_{\text{el}} = \frac{\pi K D_c}{4} \int_{-\pi/2}^{\pi/2} d\alpha \cos \alpha \sum_n n (b_n^2 + d_n^2). \quad (\text{A16})$$

The contribution arising from the host chirality turns out to be zero for symmetry reasons

$$\Delta F_{\text{chiral}} = Kq \int d\mathbf{r} \partial_y \epsilon(x, y) = 0, \quad (\text{A17})$$

which is easily inferred from inserting the expansion Eq. (A6) and integrating over y . The reduction in surface-anchoring free energy caused by the distortions Φ is as follows

$$\Delta F_{s,\Phi} = W_0 D_c^2 \cos \zeta \int_{-\pi/2}^{\pi/2} d\alpha \cos^2 \alpha \sin(2qz) \times \sum_n b_n \left(\frac{1 - (-1)^n}{n\pi} \right), \quad (\text{A18})$$

supplemented with a similar contribution accounting for the distortions ϵ

$$\Delta F_{s,\epsilon} = W_0 D_c^2 \sin(2\zeta) \int_{-\pi/2}^{\pi/2} d\alpha \cos^2 \alpha \cos^2(qz) \times \sum_n d_n \left(\frac{1 - (-1)^n}{n\pi} \right). \quad (\text{A19})$$

We find that the surface anchoring is always negative and outweighs the cost in elastic free energy thus lowering the overall free energy of the system, as it should. The results are included in Figs. 6(c) and 6(f). We find that the elastic distortions are most developed at oblique orientations (δ or $\zeta \approx \pi/4$) and do not strongly depend on the direction along which the disk is rotated.

If we now reconsider the total alignment potential for disks accounting for corrections derived above, we conclude that the ordering of the disks is hardly affected by the distortions. The free-energy changes are typically several tens of $k_B T$, which is about 2 orders of magnitude smaller than the typical Rapini-Papoular surface-anchoring free energy $W_0 D_c^2$, which is about $1500 k_B T$. disks experiencing weak surface anchoring with a cholesteric host with large pitch ($qD_c < 1$) will therefore simply follow the local molecular director with thermal fluctuations around the optimum angle being strongly suppressed. The considerable penalty incurred by angular fluctuations away from the local cholesteric director is demonstrated in Figs. 6(c) and 6(f) for a number of different host pitches. Although the presence of elastic distortions around the disk surface leads to a systematic reduction of the total free energy, their effect on the realigning properties of a colloidal disk immersed in a cholesteric host LC seems rather marginal.

[1] J. Planer, Notiz über das cholestearin, *Justus Liebigs Ann. Chem.* **118**, 25 (1861).

[2] F. Reinitzer, Beiträge zur kenntniss des cholesterins, *Monatsh. Chem.* **9**, 421 (1888).

- [3] J.-S. Wu and I. I. Smalyukh, Hopfions, heliknotons, skyrmions, torons and both abelian and nonabelian vortices in chiral liquid crystals, *Liq. Cryst. Rev.* **10**, 34 (2022).
- [4] P. J. Ackerman, R. P. Trivedi, B. Senyuk, J. van de Lagemaat, and I. I. Smalyukh, Two-dimensional skyrmions and other solitonic structures in confinement-frustrated chiral nematics, *Phys. Rev. E* **90**, 012505 (2014).
- [5] J.-S. B. Tai and I. I. Smalyukh, Surface anchoring as a control parameter for stabilizing torons, skyrmions, twisted walls, fingers, and their hybrids in chiral nematics, *Phys. Rev. E* **101**, 042702 (2020).
- [6] G. E. Volovik, Superfluid analogies of cosmological phenomena, *Phys. Rep.* **351**, 195 (2001).
- [7] M. J. Bowick, L. Chandar, E. A. Schiff, and A. M. Srivastava, The cosmological kibble mechanism in the laboratory: String formation in liquid crystals, *Science* **263**, 943 (1994).
- [8] C. Meng, J.-S. Wu, and I. I. Smalyukh, Topological steering of light by nematic vortices and analogy to cosmic strings, *Nat. Mater.* **22**, 64 (2023).
- [9] I. I. Smalyukh, Knots and other new topological effects in liquid crystals and colloids, *Rep. Prog. Phys.* **83**, 106601 (2020).
- [10] I. I. Smalyukh, Liquid crystal colloids, *Annu. Rev. Condens. Matter Phys.* **9**, 207 (2018).
- [11] K. Kamada, N. Yamamoto, and D.-L. Yang, Chiral effects in astrophysics and cosmology, *Prog. Part. Nucl. Phys.* **129**, 104016 (2022).
- [12] P. M. Chaikin, T. C. Lubensky, and T. A. Witten, *Principles of condensed matter physics* (Cambridge university press, Cambridge, 1995), Vol. 10.
- [13] M. J. Freiser, Ordered states of a nematic liquid, *Phys. Rev. Lett.* **24**, 1041 (1970).
- [14] L. J. Yu and A. Saupe, Observation of a biaxial nematic phase in potassium laurate-1-decanol-water mixtures, *Phys. Rev. Lett.* **45**, 1000 (1980).
- [15] C. Tschierske and D. J. Photinos, Biaxial nematic phases, *J. Mater. Chem.* **20**, 4263 (2010).
- [16] Q. Liu, P. J. Ackerman, T. C. Lubensky, and I. I. Smalyukh, Biaxial ferromagnetic liquid crystal colloids, *Proc. Natl. Acad. Sci. USA* **113**, 10479 (2016).
- [17] H. Mundoor, J.-S. Wu, H. H. Wensink, and I. I. Smalyukh, Thermally reconfigurable monoclinic nematic colloidal fluids, *Nature (London)* **590**, 268 (2021).
- [18] H. Mundoor, S. Park, B. Senyuk, H. H. Wensink, and I. I. Smalyukh, Hybrid molecular-colloidal liquid crystals, *Science* **360**, 768 (2018).
- [19] R. G. Priest and T. C. Lubensky, Biaxial model of cholesteric liquid crystals, *Phys. Rev. A* **9**, 893 (1974).
- [20] T. Kroin, A. M. Figueiredo Neto, L. Liébert, and Y. Galerne, Chirality-induced biaxiality at the uniaxial-to-biaxial cholesteric phase transition, *Phys. Rev. A* **40**, 4647 (1989).
- [21] J. D. Bunning, D. A. Crellin, and T. E. Faber, The effect of molecular biaxiality on the bulk properties of some nematic liquid crystals, *Liq. Cryst.* **1**, 37 (1986).
- [22] A. B. Harris, R. D. Kamien, and T. C. Lubensky, Microscopic origin of cholesteric pitch, *Phys. Rev. Lett.* **78**, 1476 (1997).
- [23] S. Dussi and M. Dijkstra, Entropy-driven formation of chiral nematic phases by computer simulations, *Nat. Commun.* **7**, 11175 (2016).
- [24] S. Dhakal and J. V. Selinger, Chirality and biaxiality in cholesteric liquid crystals, *Phys. Rev. E* **83**, 020702(R) (2011).
- [25] L. Longa, W. Fink, and H.-R. Trebin, Biaxiality of chiral liquid crystals, *Phys. Rev. E* **50**, 3841 (1994).
- [26] G. Canevari, Biaxiality in the asymptotic analysis of a 2d Landau-de Gennes model for liquid crystals, *ESAIM. Control. Optim. Calc. Var.* **21**, 101 (2015).
- [27] A. B. Harris, R. D. Kamien, and T. C. Lubensky, Molecular chirality and chiral parameters, *Rev. Mod. Phys.* **71**, 1745 (1999).
- [28] T. C. Lubensky, A. B. Harris, R. D. Kamien, and G. Yan, Chirality in liquid crystals: From microscopic origins to macroscopic structure, *Ferroelectrics* **212**, 1 (1998).
- [29] J.-S. Wu, M. T. Lázaro, H. Mundoor, H. H. Wensink, and I. I. Smalyukh, Emergent biaxiality in chiral hybrid liquid crystals, *Nat. Commun.* **15**, 9941 (2024).
- [30] M. Kléman, Defects in liquid crystals, *Rep. Prog. Phys.* **52**, 555 (1989).
- [31] O. D. Lavrentovich and M. Kleman, Cholesteric liquid crystals: Defects and topology, in *Chirality in liquid crystals* (Springer, New York, 2001), pp. 115–158.
- [32] A. Kuijk, A. Van Blaaderen, and A. Imhof, Synthesis of monodisperse, rodlike silica colloids with tunable aspect ratio, *J. Am. Chem. Soc.* **133**, 2346 (2011).
- [33] H. Mundoor, B. Senyuk, M. Almansouri, S. Park, B. Fleury, and I. I. Smalyukh, Electrostatically controlled surface boundary conditions in nematic liquid crystals and colloids, *Sci. Adv.* **5**, eaax4257 (2019).
- [34] L. Wang and Y. Li, Controlled synthesis and luminescence of lanthanide doped NaYF₄ nanocrystals, *Chem. Mater.* **19**, 727 (2007).
- [35] J. Yang, D. Shen, X. Li, W. Li, Y. Fang, Y. Wei, C. Yao, B. Tu, F. Zhang, and D. Zhao, One-step hydrothermal synthesis of carboxyl-functionalized upconversion phosphors for bioapplications, *Chem. Eur. J.* **18**, 13642 (2012).
- [36] F. Hagemans, E. B. van Der Wee, A. van Blaaderen, and A. Imhof, Synthesis of cone-shaped colloids from rod-like silica colloids with a gradient in the etching rate, *Langmuir* **32**, 3970 (2016).
- [37] I. I. Smalyukh and O. D. Lavrentovich, Three-dimensional director structures of defects in Grandjean-Cano wedges of cholesteric liquid crystals studied by fluorescence confocal polarizing microscopy, *Phys. Rev. E* **66**, 051703 (2002).
- [38] Q. Liu, Y. Yuan, and I. I. Smalyukh, Electrically and optically tunable plasmonic guest-host liquid crystals with long-range ordered nanoparticles, *Nano Lett.* **14**, 4071 (2014).
- [39] H. Mundoor and I. I. Smalyukh, Mesostructured composite materials with electrically tunable upconverting properties, *Small* **11**, 5572 (2015).
- [40] J. S. Evans, C. N. Beier, and I. I. Smalyukh, Alignment of high-aspect ratio colloidal gold nanoplatelets in nematic liquid crystals, *J. Appl. Phys.* **110**, 033535 (2011).
- [41] T. Lee, R. P. Trivedi, and I. I. Smalyukh, Multimodal nonlinear optical polarizing microscopy of long-range molecular order in liquid crystals, *Opt. Lett.* **35**, 3447 (2010).
- [42] M. Ravnik and S. Žumer, Landau-de Gennes modelling of nematic liquid crystal colloids, *Liq. Cryst.* **36**, 1201 (2009).
- [43] H. Mori, E. C. Gartland, J. R. Kelly, and P. J. Bos, Multidimensional director modeling using the q tensor representation in a liquid crystal cell and its application to the π cell with patterned electrodes, *Jpn. J. Appl. Phys.* **38**, 135 (1999).

- [44] Y. Yuan, A. Martinez, B. Senyuk, M. Tasinkevych, and I. I. Smalyukh, Chiral liquid crystal colloids, *Nat. Mater.* **17**, 71 (2018).
- [45] Y. Zhou, B. Senyuk, R. Zhang, I. I. Smalyukh, and J. J. de Pablo, Degenerate conic anchoring and colloidal elastic dipole-hexadecapole transformations, *Nat. Commun.* **10**, 1000 (2019).
- [46] W. Kutta, Beitrag zur näherungsweise Integration totaler Differentialgleichungen, *Z. Angew. Math. Phys.* **46**, 435 (1901).
- [47] D. M. Sussman and D. A. Beller, Fast, scalable, and interactive software for Landau-de Gennes numerical modeling of nematic topological defects, *Front. Phys.* **7**, 204 (2019).
- [48] H. Stark, Physics of colloidal dispersions in nematic liquid crystals, *Phys. Rep.* **351**, 387 (2001).
- [49] A. Rapini and M. Papoular, Distorsion d'une lamelle nématique sous champ magnétique conditions d'ancrage aux parois, *J. Phys. Colloq.* **30**, C4-54 (1969).
- [50] B. Senyuk, H. Mundoor, I. I. Smalyukh, and H. H. Wensink, Nematoclasticity of hybrid molecular-colloidal liquid crystals, *Phys. Rev. E* **104**, 014703 (2021).
- [51] E. Efrati and W. T. M. Irvine, Orientation-dependent handedness and chiral design, *Phys. Rev. X* **4**, 011003 (2014).
- [52] D. A. Beller, T. Machon, S. Čopar, D. M. Sussman, G. P. Alexander, R. D. Kamien, and R. A. Mosna, Geometry of the cholesteric phase, *Phys. Rev. X* **4**, 031050 (2014).
- [53] N. J. Mottram and C. J. P. Newton, Introduction to q-tensor theory, [arXiv:1409.3542](https://arxiv.org/abs/1409.3542).
- [54] N. D. Mermin, The topological theory of defects in ordered media, *Rev. Mod. Phys.* **51**, 591 (1979).
- [55] G. R. Luckhurst and T. J. Sluckin, *Biaxial Nematic Liquid Crystals: Theory, Simulation and Experiment* (Wiley, New York, 2015).
- [56] P. G. de Gennes and J. Prost, *The Physics of Liquid Crystals* (Clarendon, Oxford, 1993).
- [57] T. H. R. Skyrme, A unified field theory of mesons and baryons, *Nucl. Phys.* **31**, 556 (1962).
- [58] A. O. Leonov, I. E. Dragunov, U. K. Röbber, and A. N. Bogdanov, Theory of skyrmion states in liquid crystals, *Phys. Rev. E* **90**, 042502 (2014).
- [59] T. Machon and G. P. Alexander, Umbilic lines in orientational order, *Phys. Rev. X* **6**, 011033 (2016).
- [60] M. V. Kurik and O. D. Lavrentovich, Defects in liquid crystals: Homotopy theory and experimental studies, *Sov. Phys. Usp.* **31**, 196 (1988).
- [61] G. P. Alexander, B. G. Chen, E. A. Matsumoto, and R. D. Kamien, *Colloquium: Disclination loops, point defects, and all that in nematic liquid crystals*, *Rev. Mod. Phys.* **84**, 497 (2012).
- [62] Q. Zhang, P. J. Ackerman, Q. Liu, and I. I. Smalyukh, Interactions of micro-rods in a thin layer of a nematic liquid crystal, *Phys. Rev. Lett.* **115**, 097802 (2015).